

# Chapter 11

## Turbulent Electron Thermal and Impurity Transport

### 11.1 Validation of electron temperature gradient turbulence in the Columbia Linear Machine [*Fu, et al.* (2012)]

The electron temperature gradient (ETG) mode, which is a universal mechanism for turbulent electron thermal transport in plasmas, is produced and verified in steady-state, collisionless hydrogen plasma of the Columbia Linear Machine (CLM). Electron temperature profiles with strong gradients are produced by DC acceleration in a remote biased mesh and subsequent thermalization. Finite amplitude  $\sim 5\%$ , steady-state oscillations at  $\sim 0.3 - 0.5$  MHz (in the plasma frame), with azimuthal wave numbers  $m \sim 14 - 16$  and parallel wavenumber  $k_{\parallel} \sim 0.01 \text{ cm}^{-1}$  are measured. The massively parallel gyrokinetic toroidal code is used to study these modes. The results show that in the linear phase, the dispersion relation is consistent with kinetic theory. In the nonlinear stage, very strong nonlinear wave coupling gives rise to an inverse cascade of the energy from the fastest growing high- $m$  modes to low- $m$  nonlinear oscillations, which are consistent with the measured azimuthal mode spectrum. The radial structure of the fluctuation also agrees with the experiment. An inward radial shift of the peak of the potential fluctuation occurs during the nonlinear saturation and fluctuation fingers extend radially out to the edge plasma. Three-wave coupling mechanism is involved in the saturation of ETG modes. The simulations show a power law spectrum of the turbulence which suggests that the renormalization theory is appropriate to interpret the turbulent thermal flux.

### 11.1.1 Schematic of CLM validated ETG transport

Production and identification of Electron Temperature Gradient (ETG) turbulence modes in a steady-state cylinder with hydrogen plasma was reported in the Columbia Linear Machine (CLM) by *Wei, et al.* (2010). A measurement of electron thermal conductivity  $\chi_e(r)$  was carried out using a high-frequency triple probe giving a value of  $\chi_{\perp e}$  ranging between 2-10 m<sup>2</sup>/s, which is of the order of a several times the gyroBohm diffusion coefficient. The experimental result agreed with the value of nonlocal thermal conductivity obtained from theoretical calculations and are consistent with gyrokinetic simulation results reported in the CLM. The ETG turbulence is universal and of key importance for fusion plasmas.

A variety of drift-type instabilities relevant to toroidal magnetic fusion devices, including the trapped electron modes by *Prager, et al.* (1974), the trapped ion instability by *Slough, et al.* (1981), the collisionless curvature driven trapped particle mode by *Scarmozzino, et al.* (1986) have been produced and identified in the Columbia Linear Machine.

The drift wave driven by the radial ion temperature gradient in a collisionless cylindrical plasma was demonstrated in the modified Columbia Linear Machine (CLM) by *Sen, et al.* (1991) by using biased wire screens to create a  $T_{i\parallel}(r)$  gradient sufficient to excite an  $m = 2, 10$  kHz (in the plasma frame) drift wave oscillation. The toroidal ITG mode driven by the magnetic curvature was also produced and identified by *Chen and Sen* (1995) in the same machine.

### 11.1.2 Control of electron temperature profile

The Columbia Linear Machine (CLM) can change the electron temperature profile by adjusting the D.C. voltage of the Disc Mesh from 5 V to 20 V producing a wide range of drift waves in the plasma.

### 11.1.3 Columbia Linear Machine (CLM) profiles of electron/ion temperature and plasma density

With the appropriate values of neutral pressure and the D.C. accelerating voltage, one obtains the radial profiles of plasma density and electron/ion temperature as shown in the panel (left) in Fig. 11.1. The typical power spectrum from the high frequency twin probes is also shown (right). For flat density profiles the temperature gradient scale length  $L_{T_e}$  is the relevant parameter.

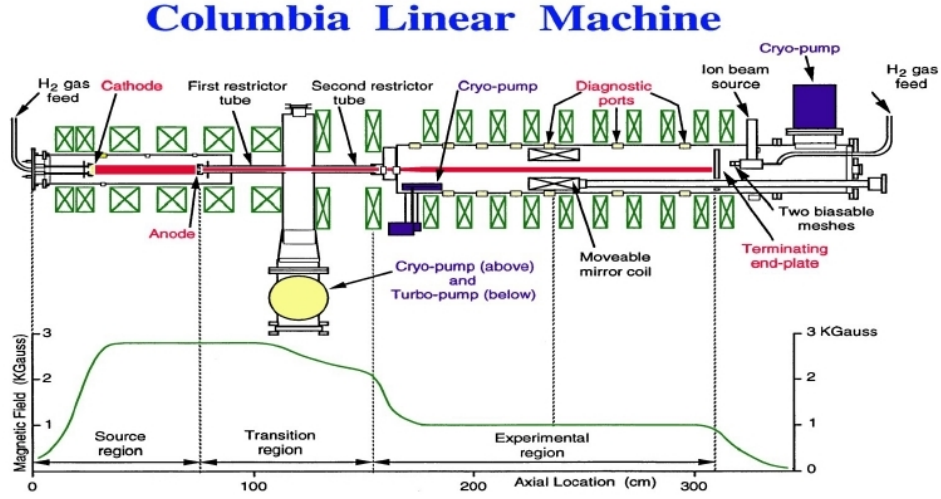


Figure 11.1: Columbia Linear Machine — Main features: steady state, collisionless, no trapped electrons flexibility for wide range of parameter variations.

#### 11.1.4 Eigenmodes from the dispersion relation

If we keep only the first-order term from the electron gyroradius and take the flat-density limit  $\omega_{ne}^* \rightarrow 0$ , the high frequency dispersion reduces to the fluid-like equation

$$\frac{T_e}{T_i} + (k_{\perp} \lambda_{De})^2 + b + b \frac{\omega_{Te}^*}{\omega} - \frac{k_p^2 v_e^2}{\omega^2} (1 - b) + \frac{\omega_{Te}^* k_p^2 v_e^2}{\omega^3} (1 + b) = 0.$$

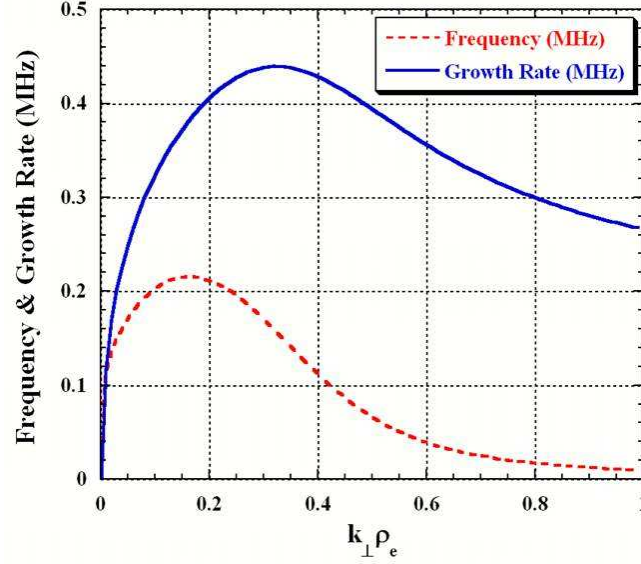


Figure 11.2: The solution of this dispersion relation is shown for measured  $L_{Te} = 0.4$  cm.

### 11.1.5 Gyrokinetic Toroidal Code (GTC) simulation results from UT-UCI SciDAC

#### GTC Simulation Results from UT-UCI SciDAC

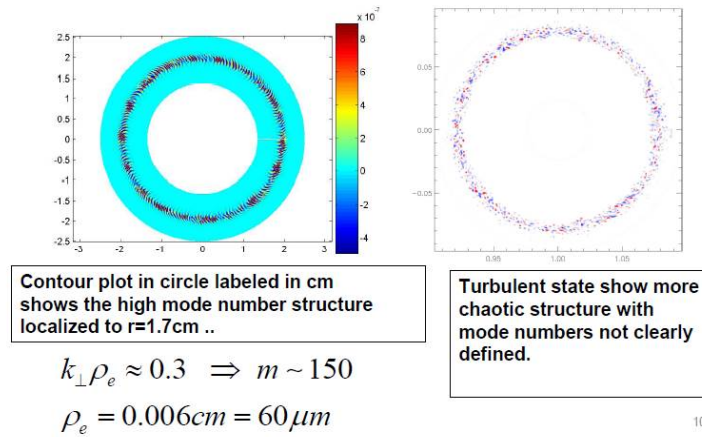


Figure 11.3: Contour plot in circle labeled in cm shows the high mode number structure localized to  $r = 1.7$  cm. (b) Turbulent state shows more chaotic structure with mode numbers not clearly defined.

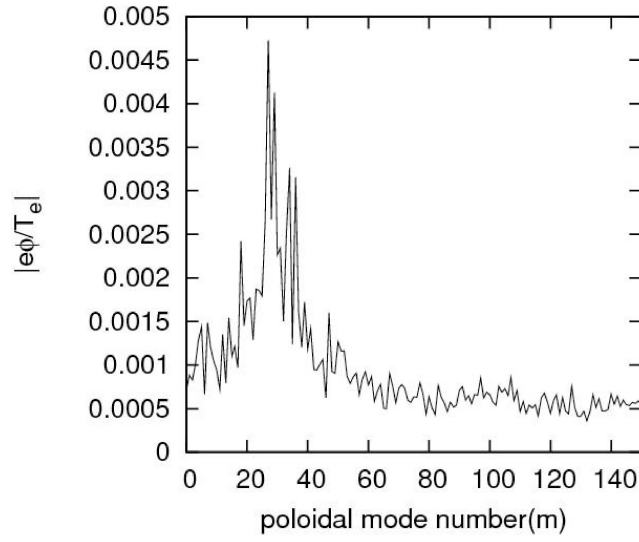


Figure 11.4: GT simulation data for model of CLM experiments.

### 11.1.6 Nonlinear quasi-steady state for $L_{T_e} = 0.5$ cm

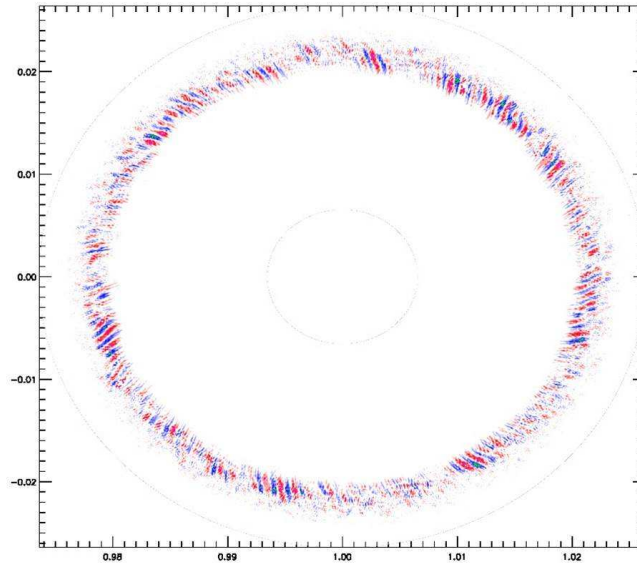


Figure 11.5: Nonlinear Quasi-Steady State for  $L_{T_e} = 0.5$  cm. Contours of electric potential fluctuations in the nonlinear state of the ETG simulation using the Gyrokinetic Toroidal Code (GTC) code. Red and Yellow = positive values. Blue and Green = negative values.

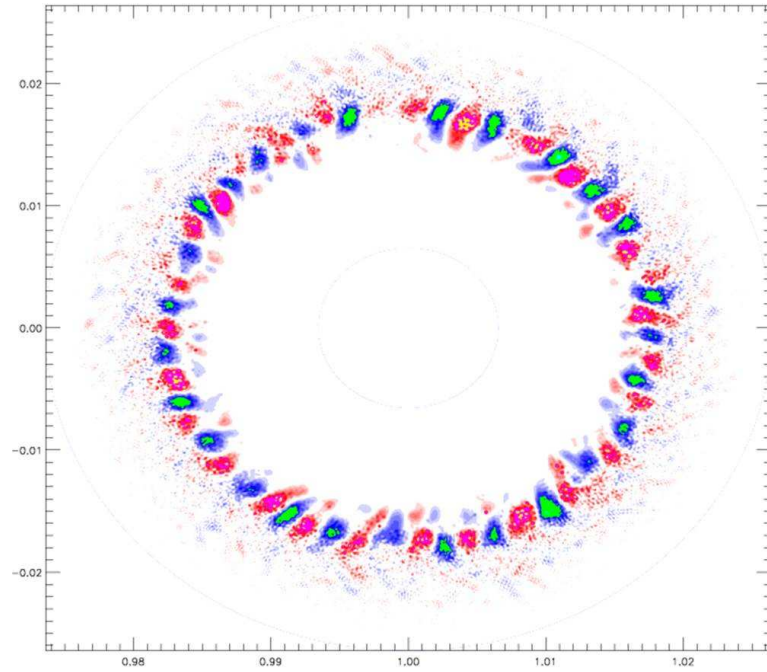


Figure 11.6: Nonlinear Quasi-Steady State for  $L_{T_e} = 0.5$  cm. Run on Teragrid Ranger TACC University of Texas. 4096 cores running 10 hours. Grid size of the simulation: 400 (radial)  $\times$  2000 (poloidal),  $\times$  32 (parallel).

### 11.1.7 Radial profiles of potential fluctuation

#### Radial Profiles of Potential Fluctuation

The maximum fluctuation level is located at the point of the sharpest electron temperature gradient ( $L_{Te}$  smallest), as predicted by theory. The width is from eigenmodes.

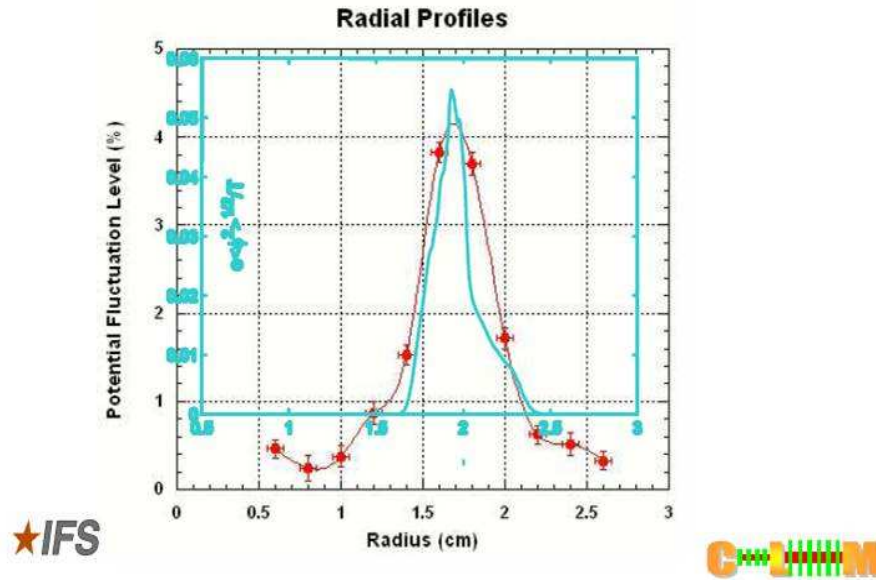


Figure 11.7: The maximum fluctuation level is located at the point of the sharpest electron temperature gradient ( $L_{Te}$  smallest), as predicted by theory. The width is from eigenmodes.

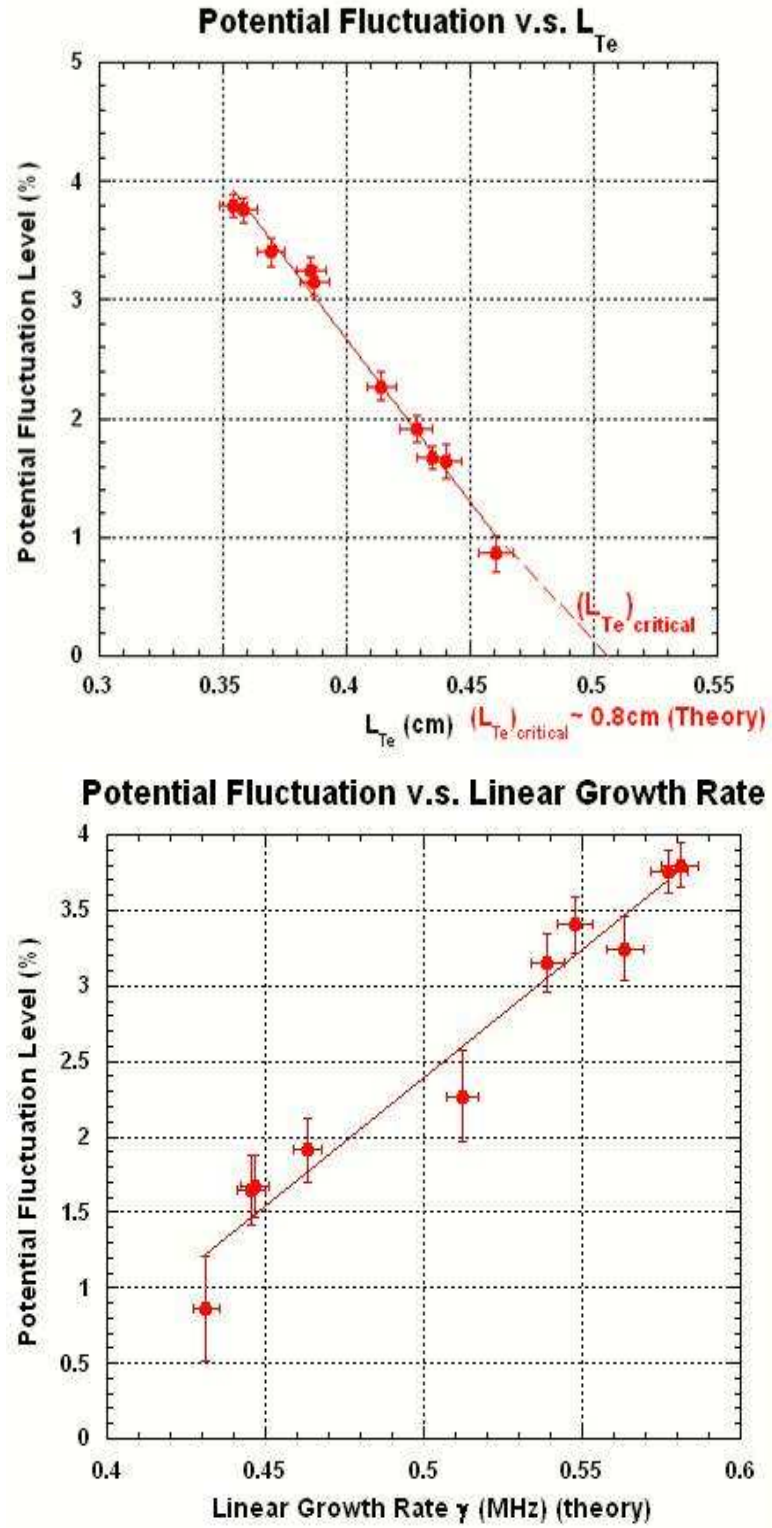


Figure 11.8: a) Temperature gradient  $L_{Te}$  Scaling. Potential fluctuation vs.  $L_{Te}$ . b) Potential fluctuation vs. linear growth rate, measured in the Columbia Linear Machine (CLM) [Fu, *et al.* (2012)].



### 11.1.8 Conclusions ETG Validation with CLM data

Potential fluctuations at approximately  $\sim 0.7$  MHz are due to the steep electron temperature gradient at relative weak density gradient. The frequency spectrum is consistent with the simulation for the ETG mode with the measured  $T_e$  profile. The maximum growth rate is at  $m \sim 90$ . The inverse cascade transforms spectrum to wave numbers  $m \sim 14-16$  as observed in the experiment where the cascade stops. The simulations and experiments show fluctuations peak for  $k_y \rho_i \geq 1$ . The unstable modes  $k_{\parallel} L_{Te} = 0.02 \text{ cm}^{-1} \times 1 \text{ cm} = .02 \langle k_y \rho_e \rangle$  for ETG instability are measured. The potential fluctuation amplitude increases linearly with  $1/L_{Te}$ . The radial location of the maximum amplitude of the mode coincides with the steepest electron temperature gradient. With the signatures described above, the ETG mode is firmly identified in the CLM with the Gyrokinetic Toroidal Code (GTC) simulations. Measurements of electron thermal conductivity indicates  $\chi_{\perp e}$  is about  $3-8 \text{ m}^2/\text{s} \approx 20 \chi_{e,GB}$  consistent with the Gyrokinetic Toroidal Code (GTC) simulations. Thus, there is validation of the Gyrokinetic Toroidal Code (GTC) simulations by the ETG experiment.

#### Impurity Transport from Drift Wave Turbulence

##### Impurity transport data and theory

Alcator C-Mod experiments with Boron and Argon and LHD, EAST, WEST experiments with trace amounts of heavy metals give important data for impurity transport.

### 11.1.9 General features of impurity transport experiments

Extensive impurity transport research has been published for plasmas in Alcator, JET, Tore Supra, JT60-U, and recently in the Chinese machines. An early work on the importance of impurity transport was the study in the Texas Experimental jTokamak (TEXT) by *Horton and Rowan* (1994). Alcator C Mod with  $R/a = 0.67 \text{ m}/0.22 \text{ m}$ ,  $B = 5.4 \text{ T}$  — confinement times 30 m. Large Helical Device  $R/a = 3.6 \text{ m}/0.4 \text{ m}$ ,  $B = 2 - 3 \text{ T}$  — confinement times 50 m.

### 11.1.10 Structure of drift wave equations with impurities

The drift waves are strongly modified by the influx of impurity ions from the plasma walls. Important impurity transport research describes the inward flux of ions from the plasma chamber walls and their crossing the magnetic separatrix [*Hidiga, et al.* (2019)].

## 11.2 General features of impurity transport experiments

Alcator C-Mod with  $R/a = 0.67\text{ m}/0.22\text{ m}$ ,  $B = 5.4\text{ T}$  — confinement times 30 ms and the Large Helical Device  $R/a = 3.6\text{ m}/0.4\text{ m}$ ,  $B = 2 - 3\text{ T}$  with confinement times 50 ms.

## 11.3 Structure of Drift Wave Equations with Impurities

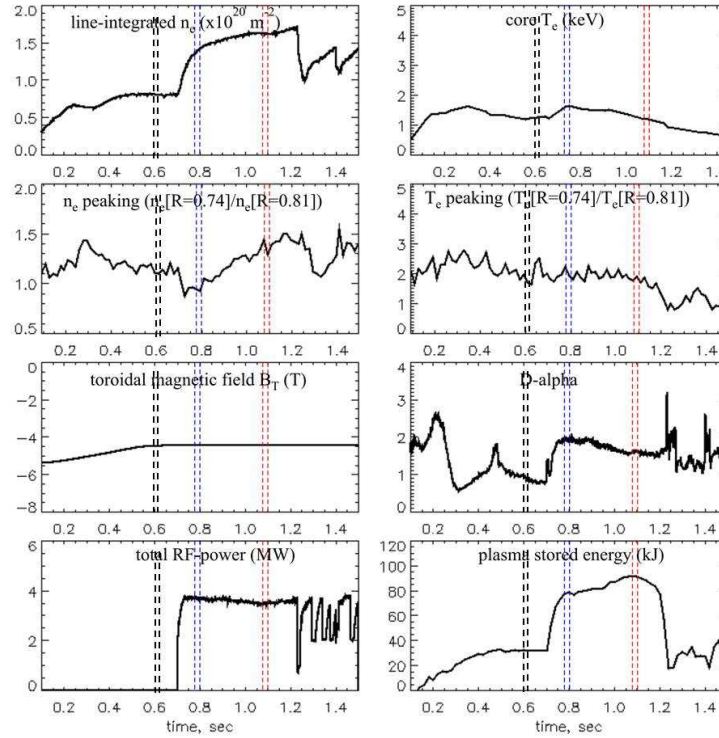


Figure 11.9: The L-mode, H-mode and ITB data in Alcator C-Mod plasmas.

H-mode is triggered by off-axis ICRF at 0.7 s. H-mode evolves to ITB after 300 msec of RF heating.

Turbulent transport due to drift waves is a critical issue for fusion physics across all magnetic confinement geometries. Three-component fluid equations are used to find the eigenmodes and eigenfrequencies of a nonuniform, magnetized plasma with a four dimensional fluctuation vector composed of fluctuations of the electron density, the working gas ion density, the impurity density, and the electrostatic plasma potential. This structure of the eigenmodes and eigenvectors is shown for two collisionality regimes: (i) the collisional drift waves appropriate for the scrape-off-layer

and the edge plasma in limiter discharges and (ii) the trapped electron mode taken in the limit of a Terry–Horton fluid description for the core plasma. From the eigenmodes and eigenvectors the part of the density and potential fluctuations that are out of phase is computed. The quasilinear particle fluxes are analyzed as a function of the power spectrum of the plasma potential fluctuations and the gradient parameters characterizing the Ohmic, H, and internal transport barrier confinement modes. A reversal in a direction of impurity flux is observed by changing the sign of the impurity density gradient length. After reversal, the impurity flux is directed outward and it is a favorable for fusion plasmas.  $B^{5+}$  density profiles start accumulating in L-mode (black), and become hollow H-mode (blue), and peaked in ITB (red) in a single discharge [Futatani, *et al.* (2010)].

## 11.4 LHD Doped Pellet Injection Data Impurity Transport Experiments

Impurity ion transport is studied in the Large Helical Device by Sudo, *et al.* (2012). A new diagnostic method with tracer–encapsulated solid pellet (TESPEL) injection with multiple tracers is developed to study impurity behaviour in a magnetically confined plasma. If a pellet contains multiple tracers, it becomes possible to compare the behaviour of different impurities simultaneously under the same plasma conditions. We injected a TESPEL into the Large Helical Device mainly with triple tracers: vanadium (V), manganese (Mn) and cobalt (Co). The Li-like lines in the vacuum ultraviolet range and the Ka lines in the soft x-ray range from these tracers are simultaneously observed with a time resolution of 50 ms. As the charges of the nuclei of intrinsic impurities, chromium (Cr) and iron (Fe), are in between those of the tracers, the behavior of Cr and Fe can be studied quantitatively by knowing the number of tracer particles and also by comparing the emission intensity change due to the electron temperature change. It is observed that the tracer impurities remain in the plasma core region when the plasma density is higher than  $5 \times 10^{19} \text{m}^{-3}$ . It is also observed that the intrinsic impurities cannot enter the core region when the plasma density is higher than the same level, although the two phenomena appear to be independent [Sudo, *et al.* (2012)].

$B = 2.7 \text{ T}$ ,  $R_{\text{ax}} = 3.7 \text{ m}$ , up to 20 MW NBI makes  $T_e \sim 2 \text{ KeV}$  and high density  $\sim 2 \times 10^{21} / \text{m}^3$ . Tracer impurity deposition from doped pellet ablation. 1 mm pellets with Fe(+26/22) and Sn(+50/21 and 18) and  $T_i(+22/18)$  and carbon injection. These high- $Z$  elements have clear spectral lines 13 nm, 16 nm, 17 nm, 19 nm with 0.6 mm spatial resolution for each pixel. Images of  $2D + t$  dynamics of the pellet spreading. Exploration of high density operation with internal diffusion barrier at  $q = 2$  surface for the 20 MW at 2.5 T experiments.

## 11.5 Features of C-Mod and LHD Impurity Transport Experiments

CMOD and LHD plasmas reach densities well above the  $10^{20}/\text{m}^3$  where extensive impurity research has been carried out. Accumulation of Boron or Carbon in some phases of discharge inward flow velocity  $V_z$  and diffusion  $-d \ln n_z/dr \equiv 1/L_{nz} \sim V_z/D_z$ . Reaching critical condition  $V_z$  can reverse and  $Z$  flow outward. Both machines, CMOD and LHD, show the  $D_z$  and  $V_z$  are well above the neoclassical values and infer that drift waves are responsible [also shown in TEXT in *Horton and Rowan* (1994)]. The problem requires a multimode approach owing to several collisionality regimes in  $r, t$  and ITG vs. TEM vs CDW transport mechanisms. A complex set of eigenmodes and eigenvectors with a new mode from  $dn_z/dr = -n_z/L_{nz}$  with both positive and negative  $L_{nz}$  values. Phase relations between the plasma density fluctuations and the potential fluctuations determine the  $D_z$  and  $V_z$ .

## 11.6 Theory-Simulation of Turbulent Impurity Transport

Three-component plasmas ( $i, z, e$ ) have additional degrees of freedom. Now, the electrons are not tied to the fuel ions so that high-density plasmas have  $\tilde{n}_e = \tilde{n}_i + \sum_z z \tilde{n}_z$  for hydrogen-working density  $n_i$ .

For each  $\mathbf{k}$ -vector, there are three eigenmodes from the pde systems:

1) hydrogen ion density, 2) impurity density, 3) electron density and 4) plasma potential

$$\omega_\alpha(k, \mu_n) = \omega_k + i\gamma_k \quad \text{polarization X}(k, \mu_n)$$

Quasineutrality (QN) reduces the system to three dynamical fields with  $a = 1, 2, 3$  eigenmodes. 10 – dim  $\mu_n$  parameter vector. Eigenmodes are worked out in detail for four generic types of discharges: L-mode, the H-mode, ITB and I-mode plasmas. Recall ITER wall is 800 m<sup>2</sup> Beryllium-coated metal tungsten. Recall Li, Be, B, B, N, O with  $Z = 3, 4, 5, 6, 7, 8$  respectively. Impurity transport at an internal transport barrier in Alcator C-Mod [*Rowan, et al.* (2008)],

## 11.7 Simulation with Atomic Physics and Impurity Fluxes in C-MOD

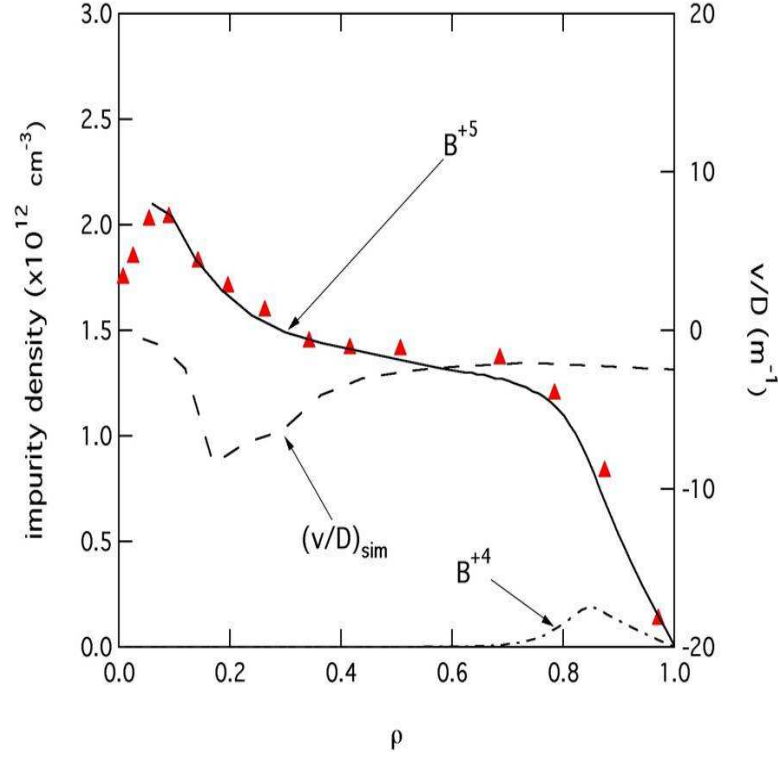


Figure 11.10: Transport Dynamics of Boron during the formation of internal transport barriers in the Alcator C-MOD impurity transport experiments [ (XXXX)].

$$\frac{\partial n_j^z}{\partial t} + \nabla \cdot \Gamma_j^z = S_j^z$$

fixed background  $n_e(r, t), n_i(r, t), T_e(r, t), T_i(r, t)$

$$\Gamma_z = -D_z \frac{\partial n_z}{\partial r} + n_z v$$

$$S_j^z = -II_n^z n_j^z n_e + I_{j-1}^z n_{j-1}^z n_e + a_{j+1}^z n_{j+1}^1 n_e - a_j^z n_j^z n_e + S_B^z$$

Alcator impurity transport measurements in Fig. 11.11 show a transition from the L-Mode radial domain where there is relatively flat  $B^{5+}$  profile.  $Z_{\text{eff}} = 1 - 1.1$  and  $T_i < T_e$  to the H-Mode radial domain where there is a hollow profile. In the hollow  $B^{5+}$  plasma  $Z_{\text{eff}} = 1.3-1.4 \rightarrow T_i < T_e$

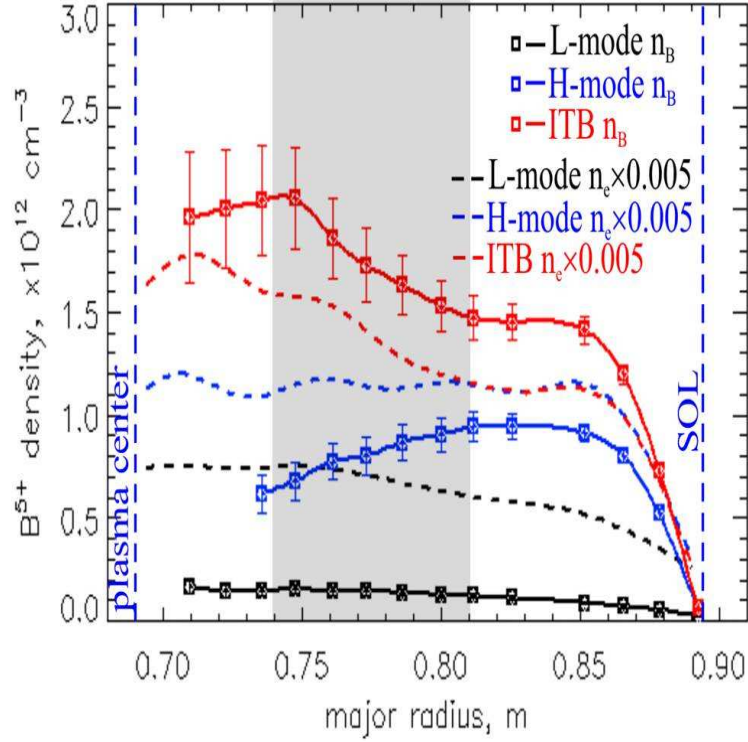


Figure 11.11: Impurity ion transport dynamics measured in the Alcator tokamak. Boron  $n$  and  $T$  profiles from CXRS on DNB. Fully stripped Boron ion,  $B^{5+}$  is the only boron ion present for  $R < 0.5$  m.

and in the ITB (inside the internal transport barrier) there is a peaked  $B^{5+}$  profile with  $T_i \approx T_e$ .

## 11.8 Carbon Transport in the LHD Machine

The Large Helical Device (LHD) is a nonaxisymmetric toroidal machine in Kyoto, Japan that has steady-state plasma. Here we show that for long steady-state NBI-driven plasmas the carbon C and Boron B densities peak in time.

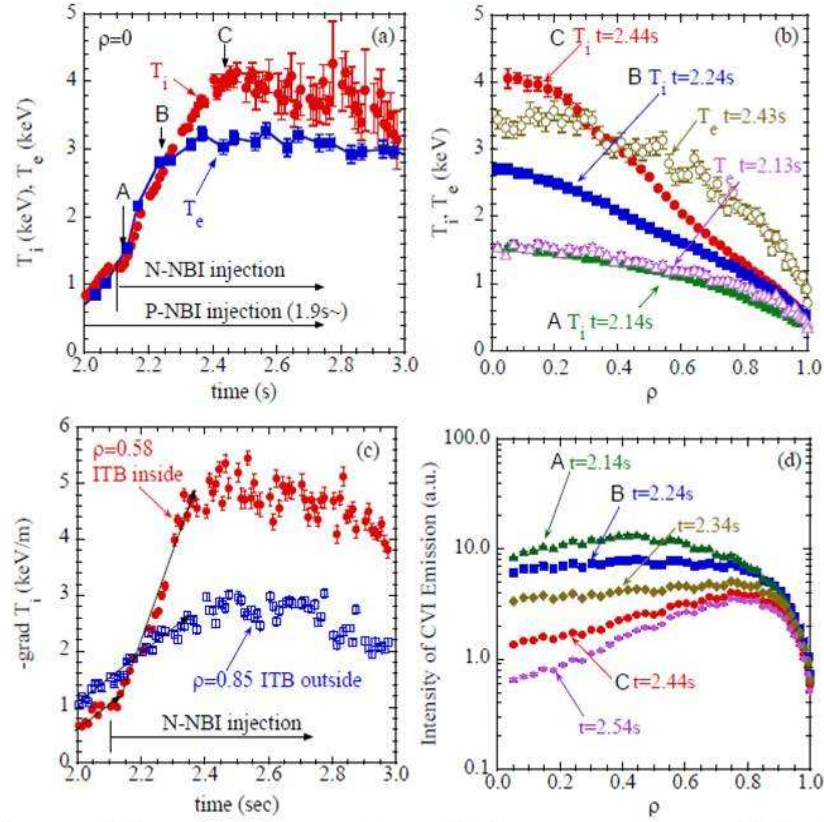


FIG. 1. (a) Time evolution of ion temperature and electron temperature. (b) Radial profiles of ion temperature and electron temperature. (c) Time evolution of ion temperature gradient. (d) Radial profiles of charge exchange emission of carbon.

Figure 11.12: Long-time evolution of the ion and electron temperatures and carbon CVI impurity density as a function of radius and time. (a) Time evolution of ion temperature and electron temperature. (b) Radial profiles of ion temperature and electron temperature. (c) Time evolution of ion temperature gradient. (d) Radial profiles of charge exchange emission of carbon.

Figure 11.13 shows the radial distributions after long times from  $t=4.1$  to  $4.4$  seconds of the temperature and the densities of the electrons and the helium, carbon and neon ions evolving in the Large Helical Device.

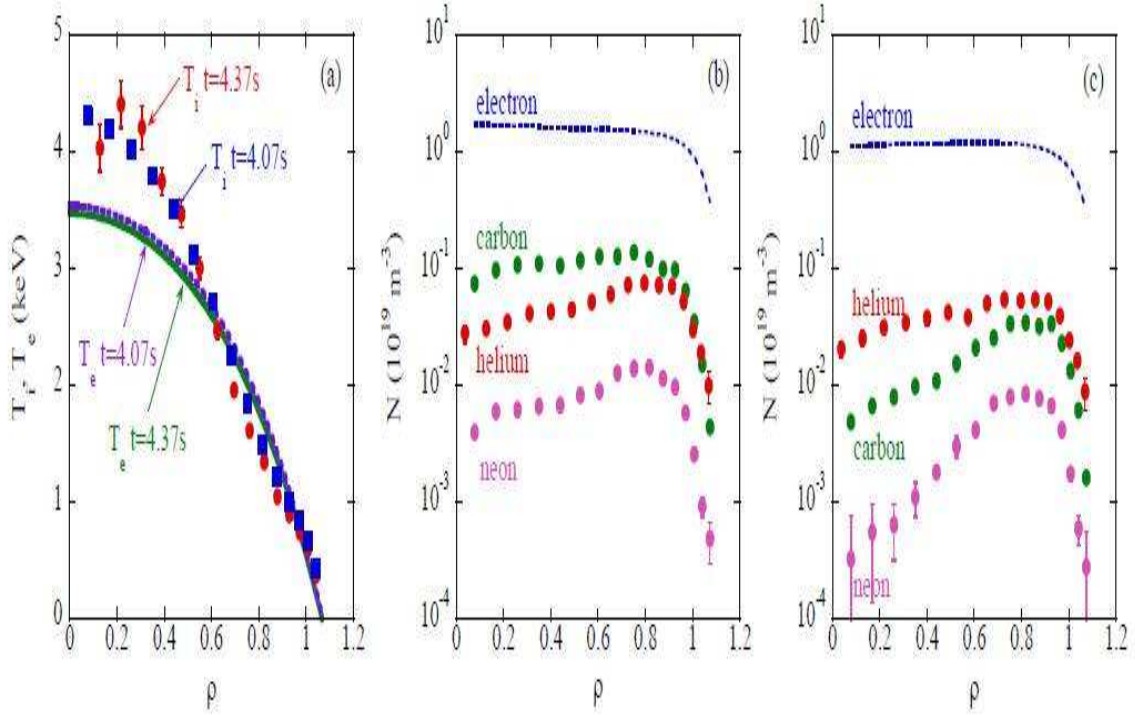


Figure 11.13: Polarization of the four fluctuation fields for the evolution of the LHD Impurity Holes.

*Yoshinuma, et al.* (2010) state as the conclusion: “Thus the observations of the impurity hole can not be explained uniformly by the neoclassical transport. The turbulence transport is therefore the candidate for the dominant mechanism for the impurity transport in the high ion temperature discharges in LHD.

## 11.9 Nonlinear 3-Component Drift Wave Model

Now we derive and carry out simulations for plasma with a general impurity density component  $z$  of density  $n_z$ .

Particle Dynamics for the three components  $n_i(x, t) + Zn_z(x, t) = n_e(x, t)$  is given by

$$\frac{dn_i}{dt} + \frac{2n_i v_x}{R} + \nabla_p n_i v_i - \nabla \cdot \left( \frac{m_i n_i}{e B^2} \frac{d}{dt} \nabla \phi \right) + \mu_i \frac{m_i}{e B^2} \nabla^4 \phi = 0 \quad (11.1)$$

$$\frac{dn_z}{dt} + \frac{2n_z v_z}{R} + \nabla_p n_z v_z - \nabla \cdot \left( \frac{m_z n_z}{Z e B^2} \frac{d}{dt} \nabla \phi \right) + \mu_z \frac{m_z}{e B^2} \nabla^4 \phi = 0 \quad (11.2)$$

and the electron density dynamics given by the Generalized Ohm's Law:  $\frac{dn_e}{dt} + \frac{2T_e}{e B R} \frac{\partial n_e}{\partial y} = \frac{1}{e} \nabla_{\parallel} \cdot J_{\parallel}$



where

$$J_{\parallel} = \sigma_{\parallel} \left( E_{\parallel} + \frac{1}{en_e} \nabla_{\parallel} P_e \right) = \sigma_P^{\text{kinetic}} \left( \frac{\partial \phi}{\partial z} + \frac{1}{en_e} \frac{\partial(n_e T_e)}{\partial x_{\parallel}} \right). \quad (11.3)$$

The coupled equations give rise to two drift waves at diamagnetic frequencies  $\omega_{j*}$  and scales  $\rho_{*j}$ .

## 11.10 Nonlinear Drift Wave Impurity Fluxes

The impurity drift waves are given by Eqs. (11.1), (11.2) and (11.3) and are derived and give the particle fluxes.

The particle fluxes are:

$$\begin{aligned} \Gamma_z &= \text{Re} \sum_k \frac{ik_y \phi_k^*}{B} \delta n_z = -n_e \frac{T_e}{eB} \sum_k \frac{k_y |e\phi_k|^2}{T_e^2} \text{Im} \hat{X}_1(k) \\ \Gamma_i &= \text{Re} \sum_k \frac{ik_y \phi_k^*}{B} \delta n_i = -n_e \frac{T_e}{eB} \sum_k \frac{k_y |e\phi_k|^2}{T_e^2} \text{Im} \hat{X}_2(k) \\ \Gamma_e &= \text{Re} \sum_k \frac{ik_y \phi_k^*}{B} \delta n_e = -n_e \frac{T_e}{\epsilon B} \sum_k \frac{k_y |e\phi_k|^2}{\tau^2} \text{Im} \hat{X}_3(k) \end{aligned}$$

where the dimensionless  $\hat{X}(k)$  functions

$$\hat{X}_{r,k} = \begin{bmatrix} \frac{\delta n_i}{n_e} / \frac{e\phi}{T_e} \\ \frac{\delta n_z}{n_e} / \frac{e\phi}{T_e} \\ \frac{\delta n_e}{n_e} / \frac{e\phi}{T_e} \end{bmatrix}$$

determine the relative transport between the impurity ions and the electrons and hydrogen ions. The polarization vectors  $\hat{X}_{r,k}$  are shown in Fig. 11.14

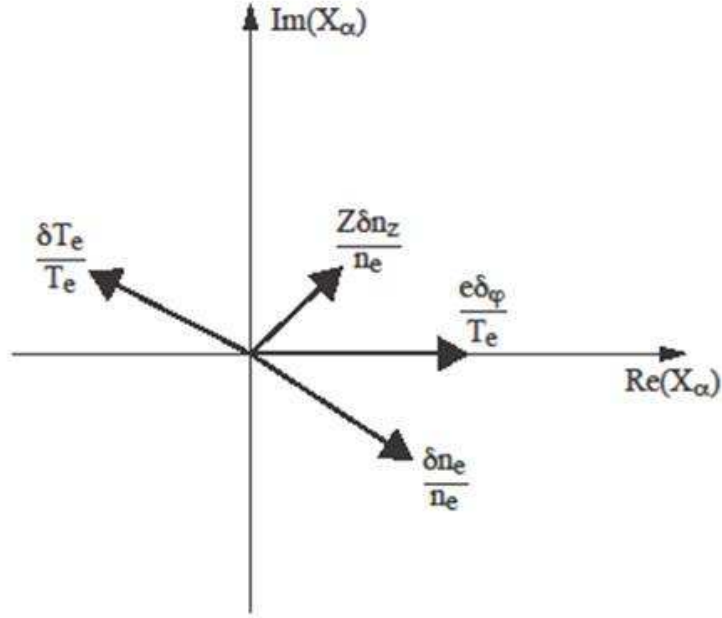


Figure 11.14: Polarization of the four fluctuation fields for the evolution of impurity holes as measured in the LHD.

### 11.11 Eigenvectors with their Relative Phases give $\mathbf{D}$ and $\mathbf{V}$ of the Impurity Holes

The three density components of the impurity fluctuation vector are shown in Fig. 11.14.

The cross correlations of  $v_x = -\frac{\partial \varphi}{B \partial y}$  with  $\delta n_s$  and  $\delta T_s$  yield the turbulent fluxes.

For particle fluxes the phase relations determine the direction of the fluxes. Introducing the phases and the neoclassical driving forces  $X_\alpha$  gives the particle fluxes

$$\Gamma_s = -D_s \frac{dn_s}{dx} + V_s n_s = -D_{\text{turb}}(W) \sum_{\alpha} [L_{s,\alpha}] [X_{\alpha}] \quad (11.4)$$

$$\Gamma_z = -D_z \frac{dn_z}{dx} + V_z n_z = -D_{\text{turb}}(W) \frac{dn_z}{dx} + \sum c_{z,n_e} \frac{R}{L_{n_e}} \quad (11.5)$$

Physically, the  $\hat{X}$  vector describes the “polarization” of density waves related to the electrostatic

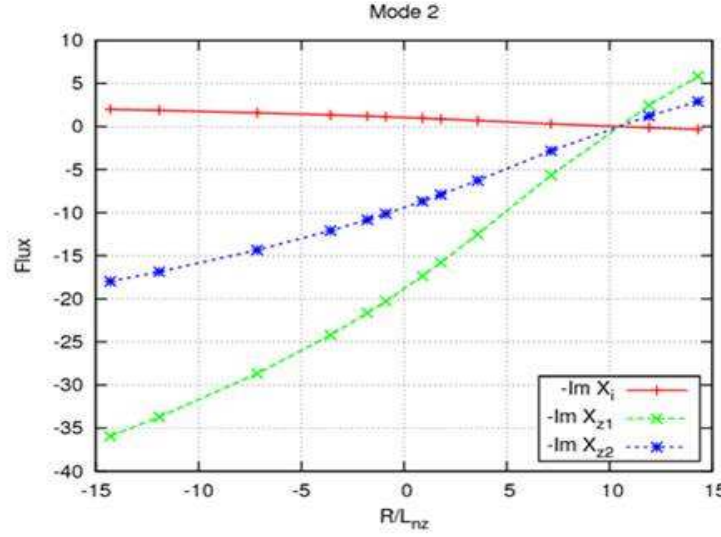


Figure 11.15: D and V fluxes from Eqs. (11.7) and (11.8).

wave. The particle fluxes are given by

$$\begin{aligned}\Gamma_i &= \text{Re} \sum_k \frac{ik_y \phi_k^*}{B} \delta n_i = -n_e \frac{T_e}{eB} \sum_k \frac{k_y |e\phi_k|^2}{T_e^2} \text{Im} \hat{X}_1(k) \\ \Gamma_z &= \text{Re} \sum_k \frac{ik_y \phi_k^*}{B} \delta n_z = -n_e \frac{T_e}{eB} \sum_k \frac{k_y |e\phi_k|^2}{T_e^2} \text{Im} \hat{X}_2(k) \\ \Gamma_e &= \text{Re} \sum_k \frac{ik_y \phi_k^*}{B} \delta n_e = -n_e \frac{T_e}{eB} \sum_k \frac{e|\phi_k|^2}{\tau^2} \text{Im} \hat{X}_3(k)\end{aligned}$$

Quasineutrality gives that  $\Gamma_e = \Gamma_i + Z\Gamma_z$ . The impurity flux is now given by

$$\Gamma_z = -D_z \frac{\partial n_z}{\partial x} + V_z n_z \quad (11.6)$$

where

$$D_z = \sum_k \frac{v_x^2(k) \gamma_k}{B^2 (\omega_A^2 + \gamma_k^2)} \quad (11.7)$$

$$V_z = \sum_k \frac{v_x^2(k) \gamma_k}{\omega_A^2 + \gamma_k^2} \left( \frac{\omega(k) e B}{k_y T_e} \right) k_\perp^2 \rho_s^2 \quad (11.8)$$

where  $v_x^2(k) = k_x^2 |phi_k|^2$ . Figure 11.15 shows an example of the three particle fluxes as a function of the impurity density gradient  $R/L_{nz}$  for a reference value of the potential fluctuation.

## 11.12 Eigenmodes and Eigenvectors for the Impurity Modes

Now we analyze the wavenumber variation of the impurity waves. Eigenmodes and eigenvectors of the linearized dynamical equations: fluctuations for a typical hollow impurity density profile are shown in Figs. 11.16.

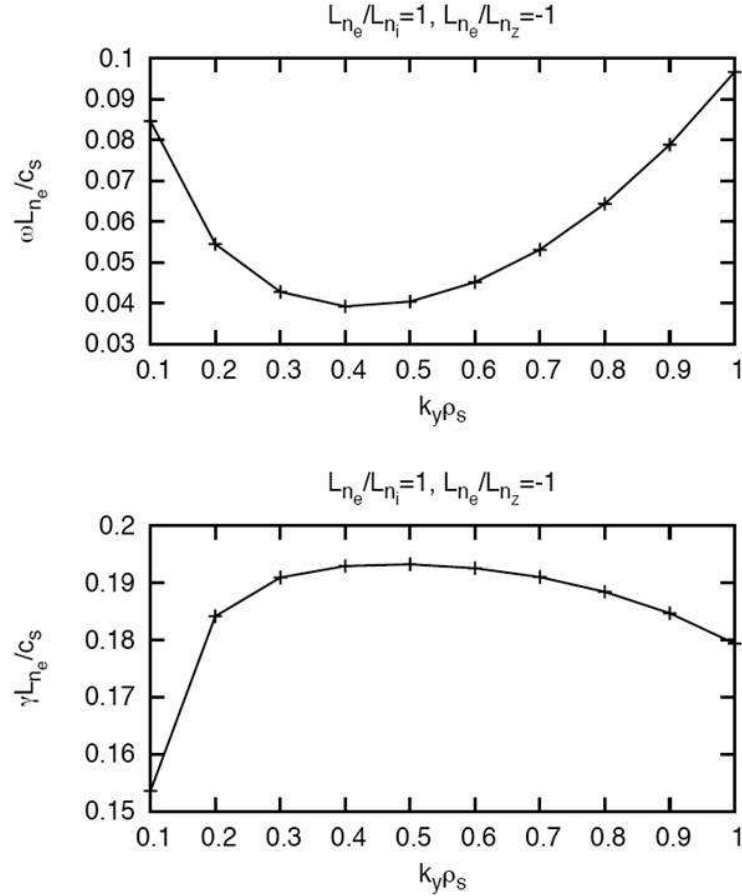


Figure 11.16: Hollow Impurity Profile:  $L_{ne}/L_{ni} = 1$ ,  $L_{ne}/L_{nz} = -1$ .

The dynamics yield the  $a$  matrix  $A(k, \omega)$  for the field vector  $X^T$

$$A(k, \omega)X^T = 0 \quad X^T = \left( \frac{\delta n_i}{n_e}, \frac{\delta n_z}{n_e}, \frac{\delta n_e}{n_e}, \frac{e\phi}{T_e} \right)$$

where the components of the  $X$ -vector are computed from the  $f_{k\omega} \exp(ik \bullet x - i\omega t)$  eigenvectors. An example for a strongly-inward peaked density Boron<sup>+5</sup> density profile with  $L_{nz} = \frac{1}{2} L_{nzi}$  in a hydrogen-Boron plasma is shown in Fig. 11.17

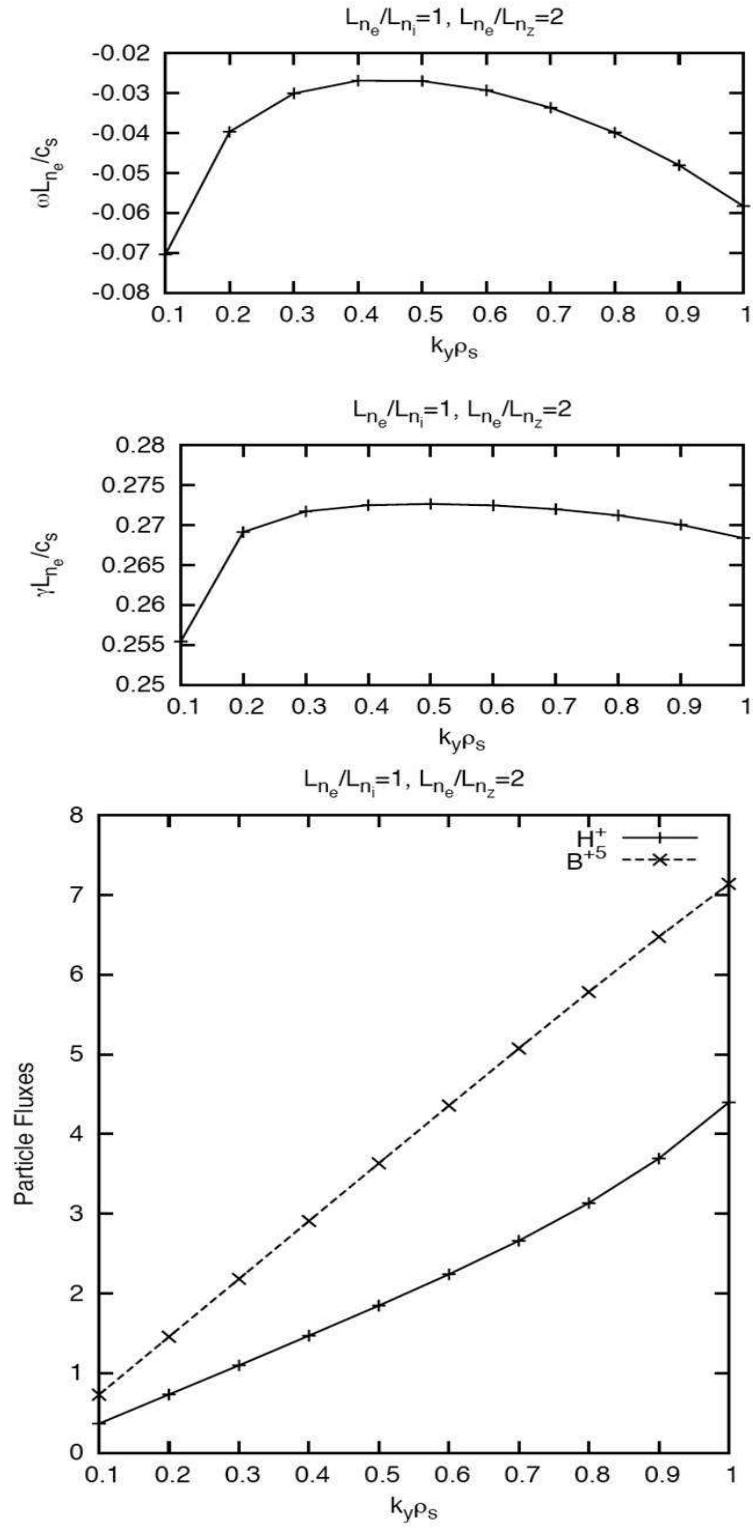


Figure 11.17: Inward-Peaked Boron<sup>+5</sup>-hydrogen plasma impurities:  $L_{ne}/L_{ni} = 1$ ,  $L_{ne}/L_{nz} = +2$ .

as a qualitative example for plasma produced in the core of the Alcator experiment in Fig. 11.11.

$$\begin{bmatrix} 1/Z & -1 & 0 & 0 \\ -i\omega & 0 & 0 & -i\omega k_{\perp}^2 \rho_{s,i}^2 + i\omega_i^* - \mu_i k_{\perp}^4 \\ 0 & -i\omega & 0 & -i\omega k_{\perp}^2 \rho_{s,z}^2 + i\omega_z^* - \mu_z k_{\perp}^4 \\ 0 & 0 & -i\omega + i\omega_{De} + k_{\parallel}^2 D_{\parallel} & i\omega^* - k_{\parallel}^2 D_{\parallel} + \mu_i k_{\perp}^4 \end{bmatrix} \begin{bmatrix} \frac{\delta n_i}{n_e} \\ \frac{\delta n_z}{n_e} \\ \frac{\delta n_3}{n_e} \\ \frac{e\phi}{T_e} \end{bmatrix} = 0$$

where the drift wave frequencies are

$$\begin{aligned} \omega_z^* &= k_y \frac{T_e}{ZeB} \frac{1}{n_e} \frac{dn_z}{dx} & \omega_i^* &= k_y \frac{T_e}{eB} \frac{1}{n_e} \frac{dn_i}{dx} \\ \omega_i^* &= -k_y \frac{T_e}{eB} \frac{1}{n_e} \frac{dn_e}{dx} & \omega_{D\alpha} &= k_y \frac{2T_{\alpha}}{eBR} \cos \theta. \end{aligned}$$

### 11.13 High- $Z$ Trace Impurity Transport as Passive Scalar

The impurity particle flux and radial electric field are given by  $\Gamma_z = -D_z dn/dr + \mu_z n Ze E_r$  [Horton and Rowan (1994)] Radial electric field gives the impurity transport — Scandium blow-off in TEXT and Pellet Injection in LHD with V, Mn and Co. For the  $E_r > 0$ , the impurity convection is outward and the impurity density is hollow due to the positive radial electric field.  $E_r(r, t)$  is complicated and largely unmeasured. High-ion temperature gradient gives negative  $E_r < 0$  with inward convection of impurities in C-Mod and others.

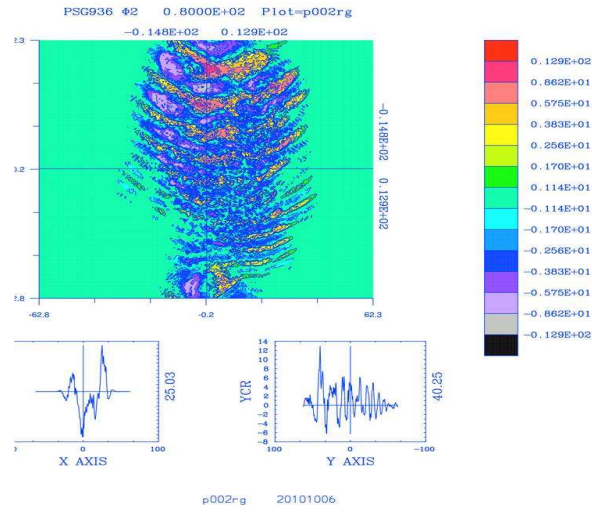
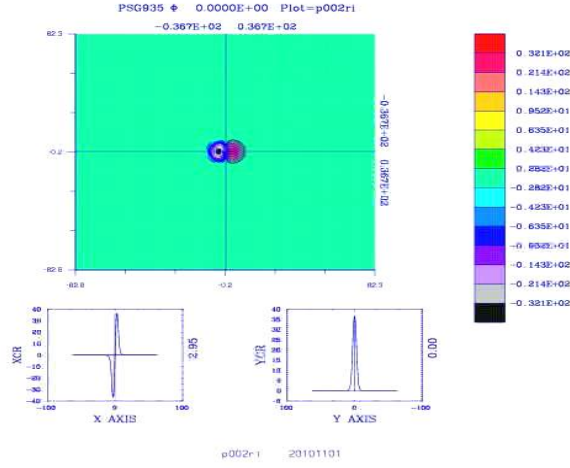


Figure 11.18: Turbulent simulation for the nonlinear turbulent spreading of impurities. Simulations from small injected “spot” of impurities as occurs from injected pellets.

Analysis shows  $D \sim (20\rho_s)^2/2 \times 50 a/c_s = 4D_{gB}$  and  $V \sim 10\rho_s/50a \sim 0.2(\rho_s/a)$  and  $V_t$  gas releases.

## 11.14 Summary and Conclusions for Impurity Transport

Impurity flux  $\Gamma_z$  is parameterized by two functions: the diffusivity  $D_z$  and advective  $V_z$  velocity giving  $\Gamma_z = -D_z \nabla n_z(r, t) + V_z n_z(r, t)$ . Turbulence theory yields the structure for the impurity flux with explicit formulas for  $D_z$  and  $V_z$  from the eigenmode/eigenvector polarizations. Neoclassical impurity fluxes are low. One needs drift waves to explain data in both C-Mod and LHD. Impurity transport with TESPEL experiments is measured and explained by theory.

## 11.15 Ion ITB Discharges in the Large Helical Device (LHD) with Impurity Transport

For the Large Helical Device (LHD) toroidal machine at NIFS in Japan extensive impurity transport studies were carried out called TESPEL. TESPEL is short for Test Pellets.

The TESPEL impurity transport experiments were performed and extensively measured correlated with theory and simulations.

The LHD plasma has three high-energy beam lines driving the plasma. One negative NBI beam energy of 180 KeV injected parallel  $B$  providing electron heating and two positive NBI beams with energy of 40 KeV energy beams injected more nearly perpendicular to  $B$  provides ion heating and from the CX Spectroscopy diagnostic.

Ion temperature, toroidal flow velocity, and poloidal flow velocity are inferred from the charge exchange emission CXRS from injected carbon.

The electron continuity equation gives

$$e\delta(nu_{\parallel}) = \frac{\omega - \omega_{*e}}{k_{\parallel}} e\delta n.$$

Ampere's Law gives the magnetic fluctuations

$$\delta B_x = \frac{1}{ik_y} \mu_0 \delta j_{\parallel} \simeq \frac{\mu_0 e n (\omega - \omega_{*e})}{ik_y k_{\parallel}} \frac{\delta n}{n}.$$

So for TS we estimate the fluctuation parallel plasma current with

$$\delta j_{\parallel} \sim 5 \times 10^6 \text{ A/m}^2 \left( \frac{\delta n}{n} \right)$$



and the fluctuating magnetic field

$$\delta B_x = 5 \times 10^{-2} T \left( \frac{\delta n}{n} \right).$$

The fractional perturbation magnetic and density fluctuations are given by

$$\frac{\delta B_x}{B} = \frac{\mu_0 e n \omega_*}{2 k_y k_{\parallel}} \frac{\delta n}{n} = \frac{\mu_0 n T_e}{2 B^2} \frac{1}{k_{\parallel} L_n} \frac{\delta n}{n} = \frac{1}{4} \frac{\beta_e}{k_{\parallel} L_n} \frac{\delta n}{n} \sim 5 \times 10^{-4},$$

and the associated magnetic stochastic transport gives the effective turbulence-driven electron thermal diffusivity

$$\chi_e^{\text{RR}} = \frac{\pi v_e}{|k_{\parallel}|} \left| \frac{\delta B_x}{B} \right|^2 \sim \frac{\pi 10^7 \text{m/s}}{10^{-2} \text{m}^{-1}} 25 \times 10^{-8} \sim 10^2 \text{m}^2/\text{s}.$$

The calculations and estimates are consistent with the LHD in impurity transport experiments.

## 11.16 ETG Modeling of NSTX with HHFW Heating in High-Beta Regime

The National Spherical Tokamak Experiment (NSTX) is described in *Kaye, et al.* (2007, 2013) and *Horton, et al.* (2005) and shows that there is a dominance of the radial magnetic turbulence  $\langle \delta B_x^2 \rangle$  in producing the measured electron thermal transport  $\chi_e(r, t)$ . The measured electron temperature profiles as a function of the applied electron heating power leads to an extensive data basis [*REF?* (XXXX)] of the electron thermal diffusivity  $\chi_e$ . The measured  $\chi_e(r, t)$  is best correlated with the Rosenbluth–Rochester  $\chi_e^{\text{RR}}$  formula [Eq. (11.9)]

$$\chi_e^{\text{RR}} = \frac{\pi v_e}{|k_{\parallel}|} \left| \frac{\delta B_x}{B} \right|^2 \sim \frac{\pi 10^7 \text{m/s}}{10^{-2} \text{m}^{-1}} 25 \times 10^{-8} \sim 10^2 \text{m}^2/\text{s} \quad (11.9)$$

from the magnetic turbulence  $\langle \delta B_x^2 \rangle$ .

The correlation of the measured electron thermal diffusivity  $\chi_e(r, t)$  with beam injection and CHERS and soft X-ray S×R day is shown in Fig. 11.19 from *Le Blanc, et al.* (2004). The measured electron transport consisted with the  $\chi_{es}^{\text{RR}}$  in Eq. (11.9) from the ETG-driven drift wave turbulence.

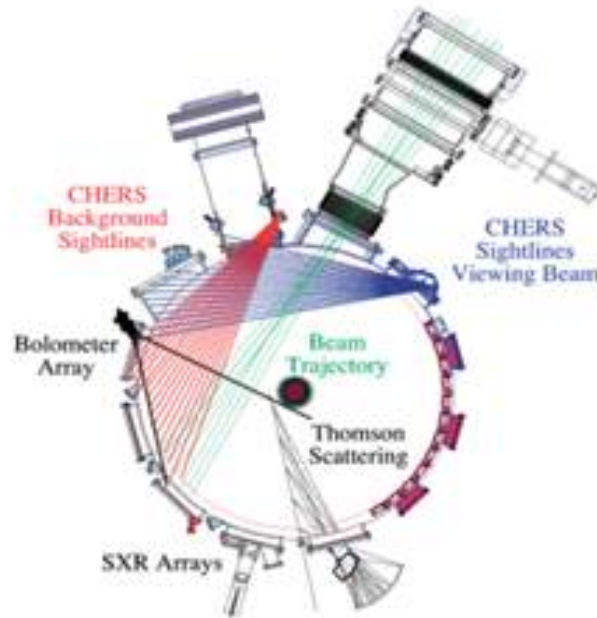
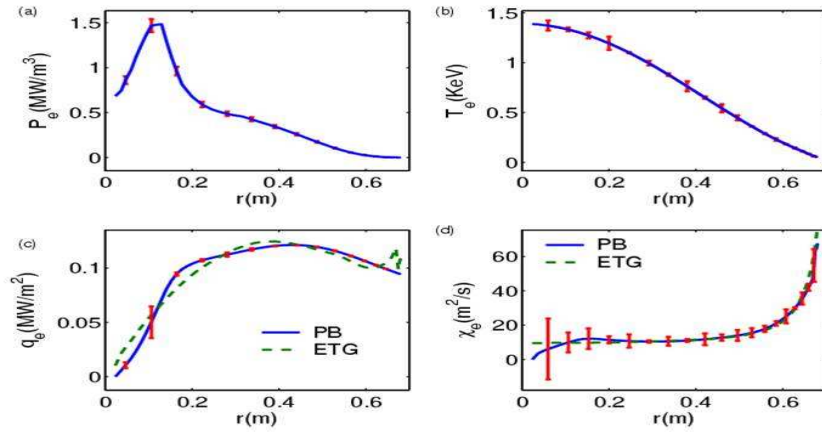


Fig. 2

Figure 11.19: a) 106194 discharge from *Le Blanc, et al. Nucl. Fusion* (2004) and *Horton, et al. Nucl. Fusion* (2005). b) RF heating is up to an order of magnitude larger than the Ohmic heating. The plasma current is essential to the confinement properties.

ETG gyrofluid simulations for modeling high- $k$  scattering data at  $k_x \rho_e = 0.13$  and  $k_y \rho_e \ll 1$  on Mazzucato scattering on NSTX [Mazzucato, *et al.* (2008, 2009)].

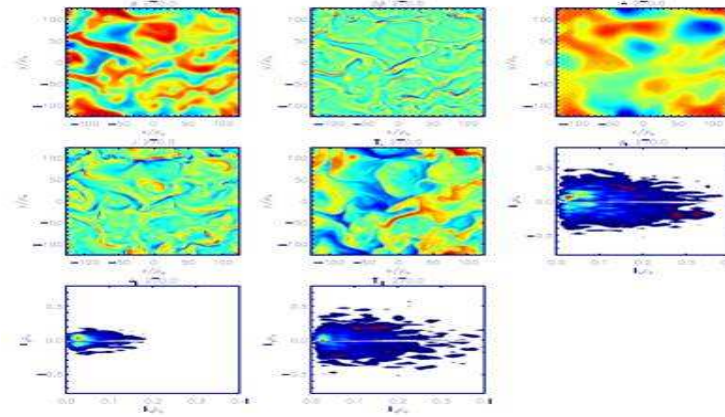


Figure 11.20: Shows formation of streamers both in the flow field and in the perpendicular magnetic field. Multiscale turbulence with intermittency in the turbulent heat flux  $q_e(t)$ . Thermal diffusivity reaches 50 to 60 times the electron-gyroBohm level. Box size is  $3\rho_i \times 3\rho_i (\sim 126\rho_e)$  time scale  $500 L_{Te}/V_e \sim 100\mu s$  (Mazzucato, *et al.* (2008, 2009)).

ETG plays the key role in determining electron transport at low  $B_T$  in the NSTX experiments.

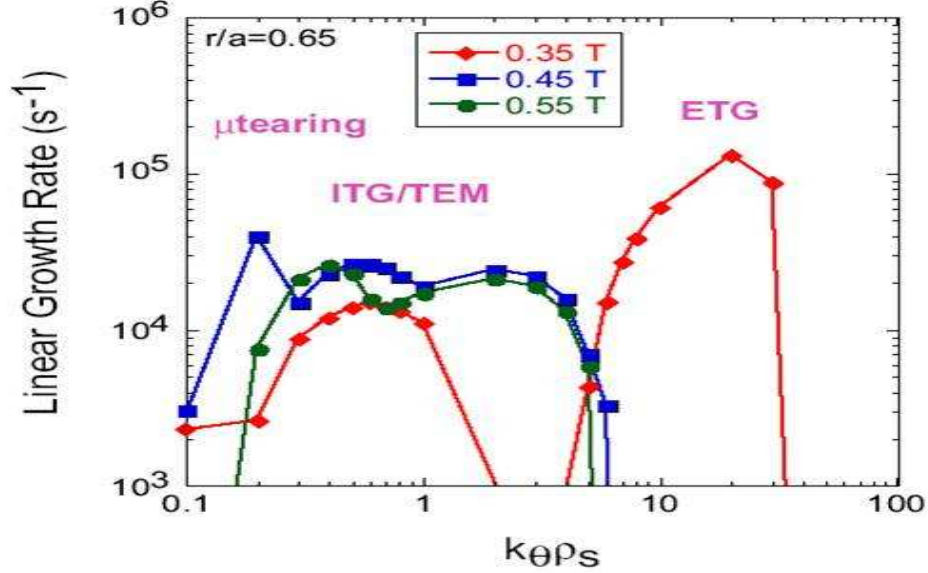


Figure 11.21: ETG linearly unstable only at lowest  $B_T$ .  $-0.35\text{ T}$  :  $R/L_{Te}$  20% above critical gradient.  $-0.45, 0.55\text{ T}$  :  $R/L_{Te}$  20-30% below critical gradient.

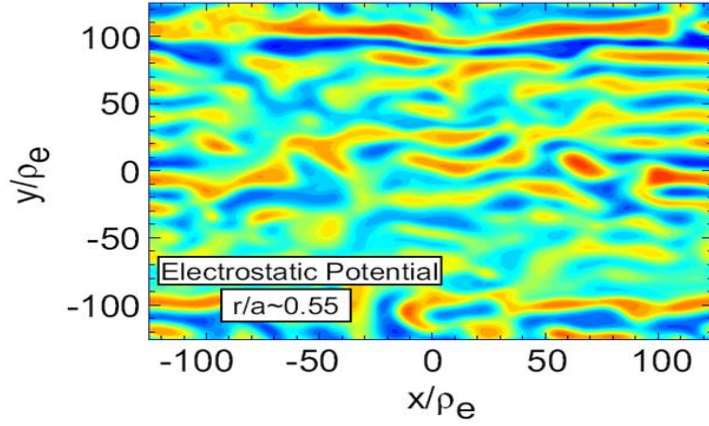


Figure 11.22: Nonlinear simulations of the ETG turbulence in the NSTX experiments are shown in Fig. 11.22.

Good agreement is found between the experimental  $\chi_e$  and the theoretical saturated transport level  $\chi_e(x, y, t)$  at 0.35 T. The experimental  $\gamma_e$  profile is consistent with that predicted by electromagnetic ETG theory (*Horton, et al. (2004)* at  $B = 0.35$  T–high beta discharge.

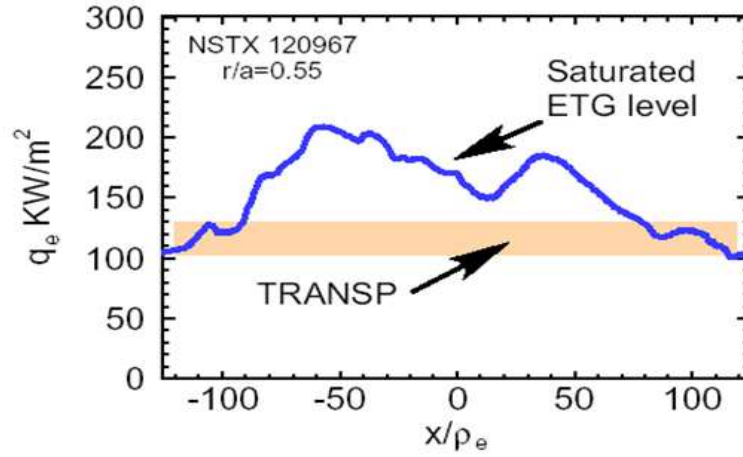


Figure 11.23: Figure 11.23 shows a comparison of the electron thermal flux  $q_e$  [Kw/m<sup>2</sup>] inferred from the diagnostic data with the TRANSP computer code and the ETG thermal flux  $q_e$  computed with nonlinear simulations.

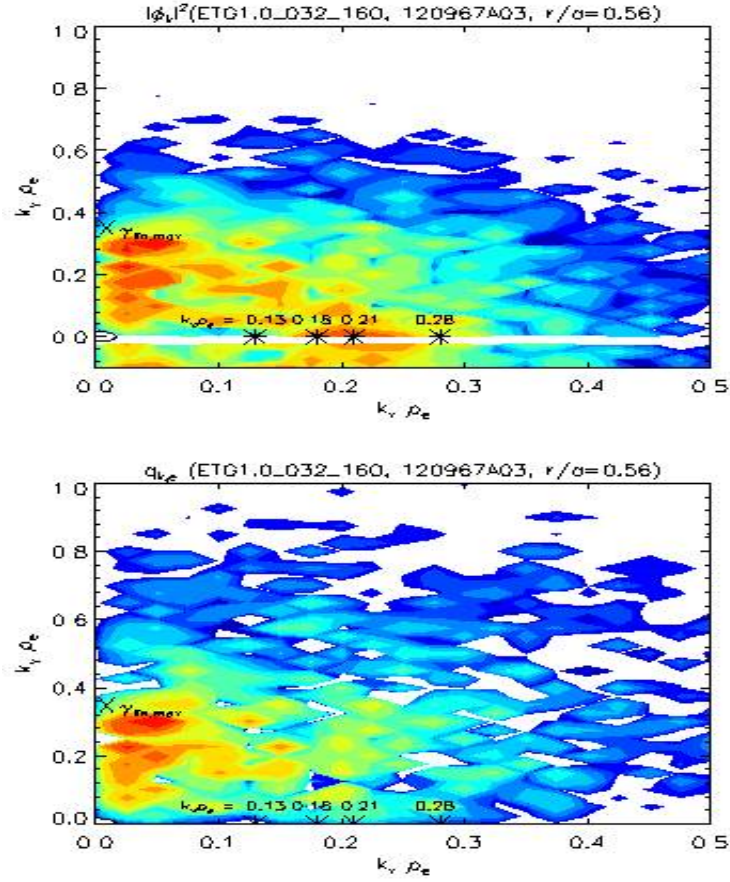


Figure 11.24: NSTX scattering data from H. Park in *S. Kaye, et al.* Chengdu IAEA, NF.

Simulations for ETG fluctuations in TCV.

## 11.17 ETG and ITG–TEM Driven Electron Thermal Fluxes

Here we review the electron thermal flux formulas that best explain the tokamak electron temperature profiles. For  $\eta_e > \eta_{e,\text{crit}}$  the electron thermal flux is

$$q_e = C_e^{\text{em}} n_e T_e \frac{c^2}{\omega_{pe}^2} \frac{v_e}{R^2} \left( \frac{R}{L_{Te}} - \frac{R}{L_c} \right)$$

For  $\eta_e > \eta_{e,\text{crit}}$  and  $\beta_e > \beta_{e,\text{crit}} = \beta_{e,\text{crit}} = \text{const} \times \frac{L_{Te}^2}{q^2 R^2}$

$$q_e = C_e^{\text{es}} n_e T_e q^2 \left( \frac{\rho_e^2 v_e}{L_{Te}^2} \right) \left( \frac{R}{L_{Te}} - \frac{R}{L_c} \right).$$

For lower  $\beta_e$  the flux is given by the ITG–TEM  $e$ –flux

$$q_e = -n_e f_{tr,e} c^{\text{ITG}} \sigma_{T_i} \frac{c_s q_s^2 \rho_s^2}{L_{T_i} R} \left( \frac{R}{L_{T_i}} - \frac{R}{L_c} \right)$$

as reviewed in *Ottaviani, et al.* (1997).

## 11.18 Conclusions for the Electron Thermal Fluxes Driven by Turbulence

Electron temperature gradient driven turbulence is documented in basic physics experiments in the steady–state, linear CLM experiments.

First Principles GTC (gyrokinetic simulations with generalized PIC methods) validated the ETG transport in the Coloumbian Linear Machine (CLM) data.

Nonlinear states with Coherent Structures (CS): vortices, streamers and nonlinear spreading of the fluctuations to linearly stable regions.

Experiments in Tore Supra, NSTX and TCV all show electron thermal transport driven by the ETG turbulence. Nonlinear plasma states have mixed interchange and tearing mode symmetries as reported in resistive– $g$  and ITG turbulence in the large body of plasma confinement literature. An example of the correlation of the dominant thermal transport in the Tore Supra machine as correlated with turbulence theory is shown in Fig. 11.24.

## 11.19 Electron Transport Results and Future Needs

ETG has become the standard model and plays key roles in NSTX, MAST, FTU, C–Mod, DIII–D, TCV and Tore Supra. The full ETG Model includes microtearing modes. Plasma data is consistent with  $\delta B_\perp^2 \propto \nabla T_e - (\nabla T_e)_{\text{crit}}$  from Cross–Polarization Scattering in Tore Supra. Ion–scale turbulence (TEM and ITG) produces further turbulence and transport in both the ion and electron thermal energy. Control of the turbulence level by  $E_r$ –shear is measured. Vortices, streamers, and zonal flows and by ICRF heating are observed and measured. The ion transport in NSTX and MAST is reported to be near the neoclassical level.

Simulation tools including GS2 and GKV (Watanabe) are being used to give detailed data on the structure of the ETG and Microtearing modes using the NSF TeraGrid, NERSC and Earth Simulator advanced computers.

## 11.20 Electron Transport Results and Future Plans

ETG has become the standard model and is verified to play key roles in NSTX, MAST, FTU, C-Mod, DIII-D, TCV and Tore Supra. The full ETG Model includes microtearing modes. Tearing modes are consistent with  $\delta B_{\perp}^2 \propto \nabla T_e - (\nabla T_e)_{\text{crit}}$  from Cross-Polarization Scattering measured in Tore Supra (TS)

Ion-scale turbulence (TEM and ITG) produces further turbulence and transport. Control by  $E_r$ -shear is measured. Vortices, streamers, and zonal flows and by ICRF heating are observed and measured. Ion transport in NSTX and MAST is near the neoclassical level.

Simulation tools including GS2 and GKV (Watanabe) are being used to give detailed data on the structure of the ETG and Microtearing modes using the NSF TeraGrid, NERSC and Earth Simulator advanced computers.

Theory of reversed magnetic shear induced electron transport barrier by *Horton and Morrison* (1998) continuing with Caldas, et al. <http://orion.ph.utexas.edu/~starpower> <http://pecos.ph.utexas.edu/~vortex> explains some laboratory experiments.

## 11.21 Simplified Solution and Critical Value of $L_{T_e}$

The fluid limit of the  $Z$ -functions gives a cubic linear dispersion relation for the slab ETG instabilities:

$$\omega^3 \approx -\tau \cdot k_{\parallel}^2 \cdot v_e^2 \cdot \omega_{T_e}^*, \quad \text{or} \quad \omega_{\text{ETG}} \approx \frac{1}{2} (k_{\parallel}^2 \cdot v_e^2 \cdot \omega_{T_e}^* / \tau)^{1/3} + i \frac{\sqrt{3}}{2} (k_{\parallel}^2 \cdot v_e^2 \cdot \omega_{T_e}^* / \tau)^{1/3}.$$

Requirement for the slab ETG instabilities is  $\eta_e = d \ln T_e / d \ln n \sim 2$ . With a density gradient, the threshold is controlled by  $L_p / L_{T_e} = L_p (-dT_e/dr) / dr / T_e$ . For flat density profiles the threshold is widely exceeded for ETG turbulence.

When we take the limit of the linear growth rate  $\rightarrow 0$ , the critical value of the electron temperature gradient scale length  $L_{T_e}$  required by the slab ETG instabilities with flat density profiles can be obtained as:

$$(k_{\parallel} L_{T_e})_{\text{critical}} \leq 0.14 \quad \text{from probe data: } 0.02 \text{ cm}^{-1} \times 0.8 \text{ cm} = 0.016$$

For instabilities, the electron temperature gradient scale length  $L_{T_e}$  should be below this critical value.

## 11.22 Ohm's Law and Frozen in Motion

The conditions for electrostatic turbulence versus the magnetic turbulence are largely determined by electron plasma pressure relative to the magnetic pressure  $B^2/2\mu_0$ . The NSTX and especially the TAE machines take advantage of the reduction of  $\chi_e$  at high  $\beta_e = 8\pi P_e/B^2$ .

Electron Dynamics:

$$\frac{m_e}{e} \frac{\partial j_{\parallel}}{\partial t} + enE_{\parallel}^{(A)} + \frac{B_x}{B} \frac{dp_e}{dx} + enE_{\parallel}^{(ES)} + \nabla_{\parallel} p_e = en\eta j_{\parallel}$$

Ampere's Law

$$j_{\parallel} = -\frac{1}{\mu_0} \nabla^2 A_{\parallel}$$

$$E_{\parallel}^{(A)} = -\frac{\partial A_{\parallel}}{\partial t} \quad \text{and} \quad E_{\parallel}^{(ES)} = -\nabla_{\parallel} \phi$$

$$\frac{T_1}{T_2} = \frac{m_e}{en\mu_0} \frac{1}{L^2} \rightarrow \frac{k_{\perp}^2 c^2}{\omega_p^2} = \begin{cases} \equiv 0 & MHD (m_e = 0) \\ \gg 1 & ES - DWs \end{cases}$$

at  $k_{\perp} \sim \frac{1}{\rho_s} = \frac{m_e}{m_i \beta_e}$ . Three regimes are defined by the balances

$A_{\parallel} - - - \text{resonance}$	$T_1 + T_2 + T_3 = 0$
$\phi - - - DW$	$T_4 + T_5 + T_6 = 0$
Frozen in Dynamics	$T_2 + T_4 = 0.$

## 11.23 ETG–Tearing modes with Closure for Parallel Electron Heat Flux

In the electromagnetic ETG–tearing mode turbulence the high–pressure plasma is described by

$$\begin{aligned} n\mathbf{v} \cdot \nabla T_e + \nabla_{\parallel} q_{e\parallel} &= 0 \\ \frac{\delta T_e}{T_e} &= -i \frac{\omega_{*T_e}}{\chi_{\parallel} k_y^2} \frac{e\phi}{T_e} \\ \mathbf{B} \cdot \nabla_{\parallel} T_e &= B_y(x) \frac{\partial \delta T_e}{\partial y} + \delta \mathbf{B} \cdot \nabla T_e = 0 \\ \frac{\delta T_e}{T_e} &= \frac{\omega_{*T_e}}{ck_y} \frac{ce\psi}{T_e} \end{aligned}$$

with the fluctuating magnetic field  $\delta \mathbf{B}$  dominating the magnetic turbulence. The energy release can be given an upper bound [ (XXXX)] from the Carnot cycles from  $T_e$ –gradient



Nonlinear equations for impurity ion gradient driven turbulence

### 11.23.1 Standard drift waves and trapped electron mode

For the first model of drift wave impurity density gradient driven turbulence the dimensionless partial differential equations are given by

$$\frac{\partial \tilde{n}_i}{\partial \tilde{t}} + \frac{R}{L_{n_i}} \frac{\partial}{\partial \tilde{y}} \tilde{\phi} + [\tilde{\phi}, \tilde{n}_i] - \left( \frac{\partial}{\partial \tilde{t}} \tilde{\nabla}_\perp^2 \tilde{\phi} + [\tilde{\phi}, \tilde{\nabla}_\perp^2 \tilde{\phi}] \right) = 0 \quad (11.10)$$

$$\frac{\partial \tilde{n}_z}{\partial \tilde{t}} + \frac{R}{L_{n_z}} \frac{\partial}{\partial \tilde{y}} \tilde{\phi} + [\tilde{\phi}, \tilde{n}_z] - \frac{A}{A} \left( \frac{\partial}{\partial \tilde{t}} \tilde{\nabla}_\perp^2 \tilde{\phi} + [\tilde{\phi}, \tilde{\nabla}_\perp^2 \tilde{\phi}] \right) = 0 \quad (11.11)$$

$$\frac{\partial \tilde{n}_e}{\partial \tilde{t}} + \frac{R}{L_{n_e}} \frac{\partial}{\partial \tilde{y}} \tilde{\phi} + [\tilde{\phi}, \tilde{n}_e] + \frac{m_i}{m_e} \frac{c_s}{R\nu_{ei}} \tilde{\nabla}_\parallel (-\tilde{\nabla}_\parallel \tilde{n}_e + \tilde{\nabla}_\parallel \tilde{\phi}) = 0 \quad (11.12)$$

For linear analysis, we can assume fluctuation in the form of  $\exp(i\mathbf{k} \cdot \mathbf{x} - i\omega t)$ , drop nonlinear terms (Poisson brackets), and rewrite linearized equations in the following matrix form

$$\mathbf{A}(\mathbf{k})\mathbf{X} = -i\omega\mathbf{B}(\mathbf{k})\mathbf{X}, \quad \text{where} \quad \mathbf{X} = \begin{bmatrix} \frac{\delta n_i}{n_i} \\ \frac{\delta n_{z1}}{n_{z1}} \\ \frac{\delta n_{z3}}{n_{z2}} \\ \frac{e\phi}{T_e} \end{bmatrix}$$

### 11.23.2 Innovative and Novel Computational Impact on Theory and Experiment (INCITE) impact on TAE business strategy

From a business point of view, the proposed INCITE work will accelerate learning and help to deliver scientific milestones which are required to unlock further private capital. The work will also help to mitigate experimental risk, which equates to mitigating capital risk; a key component of responsible stewardship of our invested capital. And the validated tools will allow strategic planning for the large scale funding round required for construction of the successor to C-2W, TAE's next experimental reactor concept.

TAE funds and participates in multiple supporting research and development efforts, with

domestic public partners including UC Irvine, PPPL, LLNL, TUNL, UCLA, U. Wisconsin, U. Washington, and U. Florida, and funded international partners including Nihon University, Japan, and Budker Institute of Nuclear Physics, Russia. This brings the benefits of parallelism and community resources to bear on the problem to increase the pace of research progress. It was with help from these partners that the TAE C-2 (2008–2015) and C-2U (2015–2016) programs discovered a High Performance Field-Reversed Configuration (FRC) regime [Binderbauer, *et al.* (2015)] and addressed along the way many of the issues regarding Compact Tori (CT) outlined in the US DOE sponsored Toroidal Alternates Panel report (2008) [Hill (2008)] and Research Needs Workshop [Hazeltime (2009)].

### 11.23.3 Broader scientific impact and context

The Field-Reversed Configuration (FRC) has no central conductor in the plasma, which greatly simplifies the engineering of a reactor concept compared to a tokamak. Important physics consequences are that there is no externally imposed toroidal direction to the magnetic field, and, in the FRC, the magnetic field increases on the outside of the torus, rather than decreasing as in the tokamak, which leads to favorable stability properties. The fraction of large orbit particles, known to have favorable stability properties [Rosenbluth, *et al.* (1962)] is also larger in the FRC than in other machines. Despite these differences, a important quantitative similarity has been discovered, which is that the energy transport scalings found on the larger Spherical Tokamak and FRC experiments are similar, with  $B\tau_E \sim v_{e*}^{-0.8 \text{ to } -1.0}$  for NSTX [Kaye, *et al.* (2007, 2013)], and  $B\tau_E \sim v_e^{-1}$  for C-2U [Binderbauer, *et al.* (2015)]. The meaning of these approximately  $1/v_e$  scalings is that the energy confinement per magnetic field improves as the temperature increases, which is ideal for a fusion reactor. Both NSTX-U and C-2W experimental programs have plans to study these transport scalings to see how well they extend into higher electron temperature parameter regimes. A public/private collaboration is under development to allow synergistic interaction between the two programs.

In C-2W the core toroidal magnetic field region is enveloped in an open magnetic field line region of plasma known as the Scrape-Off Layer (SOL), which is confined between two magnetic mirrors. Particles that escape through the mirrors move into the divertor expander vessels (see Fig. 2) where the magnetic field lines flare outward as in the Gas Dynamic Trap (GDT) experiment [Ivanov and Prikhodko (2013)]. There is an active collaboration between TAE and the GDT teams which is advancing the understanding of mirror plasma physics. The resulting scientific insights could have significant wider technological benefit, as there are several organizations that are exploring mirror devices as commercializable neutron sources for use in materials testing and remote sensing [Ryutov (1990), Horton, *et al.* (2010)]. The scientific community has taken note of these interesting points of comparison between the CW experiment and the NSTX-U and GDT experiments. These were highlighted at the recent DOE-backed 2016 US-Japan Compact Tori Workshop [Tajima and Asai (2016)], where members of the tokamak, Compact Torus, and mirror communities gathered to discuss synergistic physics research topics. Of particular relevance to the current INCITE proposal, this workshop concluded with a call to create a community-wide

collaboration to develop the capability for high fidelity simulation of Compact Torus plasmas, a category which includes FRCs such as TAE’s C-2W, and Spherical Tori (ST) such as PPPL’s NSTX-U.

To meet this need, the lead PI on the INCITE proposal also led in 2017 (under the auspices of UC Irvine) is a multi-institution SciDAC proposal to create a Center for Whole Device Modeling of Compact Tori (WDMCT) to support US domestic research into high beta plasmas for fusion applications. The proposal was in response to the SciDAC Whole Device Modeling FOA [*SciDAC* (2017)]. The proposal was to create a public-private partnership, where TAE would fully fund about ten FTE members of its Computational Modeling group to participate, and SciDAC would fund about ten FTE non-TAE scientists at universities, national labs, and private companies. Co-PIs on the SciDAC proposal included Jan Egedal of University of Wisconsin, Kai Germaschewski of University of New Hampshire, Burlen Loring of LBNL, and representatives of private research companies including Sergei Galkin of Far-Tech Inc, Robert Harvey of CompX Co, Yuri Omelchenko of Trinum Research, and Dale Welch of Voss Scientific. Representatives of numerous public institutions signed on to be unfunded collaborators to assist with theoretical support and experimental validation of the developed models. Unfunded theoretical and computational collaborators included Daniel C. Barnes of Coronado consulting, Elena Belova of PPPL, Toshikazu Ebisuzaki of RIKEN, Walter Guttenfelder of PPPL, Yasuaki Kishimoto of Kyoto University, Zhihong Lin of UC Irvine, and the TAE team. Unfunded experimental collaborators included Stan Kaye of the Core Science Team of NSTX-U at PPPL, Peter Bagryansky of the GDT team at Budker Institute of Nuclear Physics, Michael Brown of the SSX group at Swarthmore College, and Tomohiko Asai of the FAT-CW experimental team at Nihon University, and the TAE C-2W experimental team.

The multi-institution collaborators on the SciDAC proposal agreed that two of the highest priorities of the WDMCT Center would be the simulation of the kinetic microturbulence and the global stability. TAE’s efforts on these strategically important components of the WDM are intense. These simulation components have both been under development since 2013 with the FRC kinetic global stability code.

## 11.24 Research Objectives and Milestones

### 11.24.1 Research objectives for the TAE development program

The overarching goals are to accelerate the scientific progress of the C-2W experimental program, and to develop predictive simulations for future fusion reactor prototype concepts. The strategic simulation goal is to develop the Whole Device Model (WDM) codes.

The main goal of the C-2W experimental program is to increase the temperature of the magnetically-confined plasma and verify the energy confinement scaling  $B\tau_E \sim v_e^{-1}$  discovered on C-2U. The experimental strategy to accomplish this is to use known methods to form the plasma

in C-2U conditions, and then to ramp up the plasma parameters using external actuators. Plasma parameters will then pass from a known state space, to a new state space. This imparts some element of risk: the global stability properties of the plasma may change in the process, so feedback and control systems are built into C-2W to keep the plasma macroscopically stable. Macroscopic stability is a prerequisite for the study of the energy confinement scaling. TAE's C-2U experiment was only able to demonstrate the favorable confinement scaling after macroscopic stability had been mastered.

The two elements of the WDM are the A New Code (ANC) and Field-Reversed Configuration (FRC) codes. Together they are used to find stable operating points in new parameter regimes, and to make quantitative predictions of the turbulent transport levels. The computer simulations mitigate experimental risk inherent in the exploration of new parameter regimes, accelerate the optimization of experimental operating scenarios, and use validated models to predict the stable and efficient operating points for the next FRC reactor design named Norm — short for Norman Rostoker.

### 11.24.2 Motivation for the choice of tools

Transport in magnetically-confined plasmas is determined by underlying microturbulence, which is characterized by length and time scales less than the ion Larmor radius and cyclotron frequency dynamics. In the FRC, overall confinement time depends on a balance between the cross-field and parallel-to-field transport dynamics, and the topologically distinct core and open field-line Scrape-Off Layer (SOL) transport. Further, global features, such as plasma current and pressure gradients also provide sources of free energy which drive the microturbulence. Due to the difficulty of resolving the wide range of time scales involved, a pragmatic approach is to apply two separate simulation codes, one for long time scale macrostability and the other for short time scale microturbulence. This is the motivation for using Field-Reversed Configuration (FRC) and A New Code (ANC) computer codes. The FRC magnetic configuration has special features mentioned in Sec. 6.10, including vanishing magnetic field regions, ion orbits comparable to the device size, and high beta self-organization, which place requirements on the simulation models which are more stringent than in tokamak codes. To meet these requirements, both A New Code (ANC) and Field-Reversed Configuration (FRC) codes use fully kinetic ion orbits, and cannot make use of magnetic field-aligned coordinate systems. A high level comparison of the two codes is shown in Table 11.1, and the codes are described in the following subsections.

### 11.24.3 Macro-stability code Finite Electron Mass Particle-In-Cell (FPIC)

The Finite Electron Mass Particle-In-Cell (FPIC) code [Dettrick, *et al.* (2015)] is a 3D global plasma stability code. Fully kinetic ions are used to capture the kinetic stabilization and destabilization of global modes which is known to occur [Milroy *et al.* (1989), Belova, *et al.* (2003)].

Electron energy is represented by an equation of state, and a generalized Ohm's law is used with an optional finite electron mass correction term consisting of a vector Laplacian pre-multiplied by the ion skin depth squared. This correction affects the plasma/vacuum boundary which is usually treated by ad hoc resistivity tuning in hybrid codes. Particular care has been taken to allow realistically shaped boundaries, which can be either conducting walls or resistive plasmas.

FPIC is used to study shape and position instabilities in general Compact Tori in the presence of conducting or resistive boundaries, including kinetic ion effects, multiple ion species, and other actuators on stability such as neutral beam injection and electrode biasing. The code is used to simulate feedback and control of those instabilities using coils as magnetic actuators in the Norman and future Norm experiments.

An example of successful application of the FPIC code [Ceccherini, *et al.* (2016)] is shown in Fig. XX: the stability of the tilt mode as a function of the ion kinetic parameter  $E/S^*$  (large  $E/S^*$  is more kinetic). The left panel shows evolution of the tilt mode followed by nonlinear saturation (c.f.) [Belova, *et al.* (2004)]. The right panel shows the results of modal analysis of 13 separate simulations, compared to analytic theory [Steinhauer (2011)].

#### 11.24.4 Microstability code — A New Code (ANC)

A New Code (ANC) is a first-principles, integrated PIC microturbulence code. ANC is based on the Gyrokinetic Toroidal Code (GTC) at UC Irvine, but designed specifically for FRC magnetic geometry, to capture large-orbit ion dynamics, and cross-separatrix transport. It has been developed to investigate transport in TAE's FRC devices C-2, C-2U, and C-2W, and future reactor prototype designs.

ANC's physics model solves the Vlasov-Poisson system, including a fully-kinetic or gyrokinetic ion advance, gyrokinetic or adiabatic electrons, and corresponding Poisson solvers. The particle species distribution functions are modeled using a perturbative ( $\delta f$ ) formulation for substantially reduced particle noise. ANC's formulation uses cylindrical coordinates rather than magnetic coordinates in order to treat dynamics crossing the magnetic separatrix as well as magnetic field nulls. The ANC code is tailored to simulate FRC magnetic geometry and initialized from numerically-specified equilibrium in a TAE specific HDF5 format, which is shared with the FPIC code.

A major part of the code development is continuing cross-code verifications with GTC. The gyrokinetic ion model in ANC has been applied to perform global linear and nonlinear simulations in C-2U and other geometries, for comparison to turbulent fluctuation measurements [Schmitz, *et al.* (2016)] prior single-flux-surface GTC simulations [Fulton, *et al.* (2016) Lau, *et al.* (2017)].

Table 11.1: High-level comparison of ANC and FPIC code features and plans.

	ANC	FPIC
target physics	microturbulence	global stability; stability and control
fields	electrostatic, electromagnetic	electromagnetic
particle model	perturbative (“delta $f$ ”), fully kinetic ions, drift kinetic electrons	nonperturbative (“full $f$ ”), fully kinetic ions, fluid electrons
domain	2 + 1 D, cylindrical+Fourier; local in Fourier mode	3D Cartesian Yee mesh; global
time scale mitigation	Adiabatic or orbit averaged electrons; Light waves not tracked in electromagnetic model;	Quasineutrality; Darwin model; Faraday subcycling; Implicit methods
length scales	Debye length; ion gyroradius; electron gyroradius	ion inertial length; ion gyroradius
inter-node parallelism	MPI Group parallel	MPI domain decomposed
intra-node parallelism	MPI, OpenMP	MPI, OpenMP, CUDA

### 11.24.5 TAE research and development milestones

There are two TAE milestones per year as listed in 1 to 6 below. Each milestone is described in the text. In subsection 3.1 milestones are also broken into Research and Development tasks, recorded as subitems a,b,c etc. Year in which task or milestone is to be accomplished is designated by Y1, Y2, or Y3.

1. Verification of model components (Y1). Both ANC and FPIC will undergo additional analytical and cross-code verifications, to ensure that the model implementations accurately reflect their physics formulations. In ANC, some early optimization work on the spline algorithm will also be performed, to speed up the subsequent milestones.
2. Validation of model components against experiment (Y1). ANC and FPIC simulations will be compared to experimental data to validate that their models are sufficient to describe the real FRC. ANC transport simulations will be compared to fluctuation data from the completed C-2U campaign as well as prior GTC simulations, and FPIC will perform a positional stability scan against data from the new C-2W device.
3. Initial C-2W stability and transport calculations (Y2). The crux of this proposal is supporting the new C-2W device at TAE. In this milestone, ANC will perform a complete global,

nonlinear transport calculation, providing values for heat and particle flux, while FPIC will study stability dependence on a variety of equilibrium properties and C-2W actuators.

4. Refinement of models and algorithms (Y2). The model will enter a development phase, based on difficulties discovered in milestones 2 and 3. Key items we anticipate adding are magnetic perturbations in ANC and an implicit algorithm in FPIC which may provide  $\sim 10\times$  speedup.
5. Advanced C-2W stability and transport calculations (Y3). The C-2W simulations performed in Milestone 3 will be re-performed using the refined model, including all new actuators in FPIC and magnetic perturbations in ANC.
6. Future reactor prototyping simulations (Y3). The FRC stability and transport model will be applied to future reactor concepts in an exploratory fashion, primarily to direct future code development and mitigate experimental risk.

### 11.24.6 TAE publications

After a beginning period of operating in stealth, TAE has grown to value interaction with the wider plasma physics community. Following recent published work on transport in C-2U [Schmitz, *et al.* (2016)] and numerous more recent publications. Topics include respective formulations of ANC and FPIC, comparison of gyrokinetic and fully-kinetic ion models in the FRC, simulation of drift-wave turbulence in global FRC geometry, beam driven instabilities, and feedback and control simulations.

For ANC simulations, the estimates are to use 2048 nodes, so a 1 MCH linear simulation would take approximately 7.6 hours on 2048 nodes, while nonlinear simulations would be intensive, taking approximately 150 hours on 2048 nodes. Restarts and check pointing are implemented and will be utilized for longer ANC simulations. For FPIC, planned usage is with 512 Theta nodes. Typical production run requires 0.5 M core hours, or 512 nodes for approximately 15.3 hours.

Time estimates for the ANC simulations are generated using a value of [MCH/time step] determined empirically by running the representative case discussed in Subsection 3.3.1 and in Fig. 3.7. This case uses a realistic FRC magnetic geometry, with an intermediary problem grid size. Time estimates are scaled proportionally to the number of grid points appropriate for C-2W or C-2U equilibrium and with sufficient physics resolution (approximately  $10 \times \lambda_{\text{Debye}}$ ) which is conservatively sufficient for the formulation. For linear simulations, the number of required time steps is then estimated by assuming the time step size is  $(1/20)$  of the ion gyroperiod, and that the physical time elapsed is  $(5)$  oscillation periods of the real frequency,  $\omega_r$ , of the phenomenon of interest. This results in a total number of time steps  $0.01 \times \Omega_{ci}/\omega_r$ . In the case of ion acoustic waves and ion Bernstein waves  $\omega_r$  is estimated analytically. For the linear C-2U and C-2W scans,  $\omega_r$  is estimated from experimental observations and from prior gyrokinetic simulations. Nonlinear ANC simulations are roughly estimated to be ten times more expensive than their linear counterparts. This is based on using the same grid resolution, with five times longer simulations, to allow linear

growth times followed by nonlinear saturation states and several times more particles per cell, which is required to reduce noise in the nonlinear state.

FPIC time requirements for typical C-2W production simulations are estimated from the strong scaling studies. Optimal node count is determined from the sweet spot in Fig. 3.8, which is at 512 Theta nodes, at which point each time step takes about 5 seconds (reading from the figure). This is for a typical production scenario which has  $10^6$  cells and  $10^9$  particles advanced for  $0.54e$  steps. There are  $\sim 10^6$  cells because the ion skin depth is  $\sim 3$  cm and the simulation domain is 1.6 m diameter and 8 to 12 meters long. There are  $\sim 10^3$  particles per cell because FPIC is nonperturbative and electromagnetic. There are  $\sim 10^4$  time steps per run because the time advance is explicit, the time step is determined by the fastest Alfvén speed which is set by high-field, low-density regions under the mirror, making the time step around  $10^{-8}$  seconds, and the code should be integrated for  $\sim 10^{-4}$  seconds in order to observe linear growth of instabilities and subsequent saturation. A typical  $10^6$  cell,  $10^9$  particle,  $0.54e$  time step production run takes 5 seconds per step and therefore requires 7 hours of wall time, and approximately 0.25 million Theta core hours (0.75 million Mira core hours equivalent) on 512 nodes. As a rule of thumb, a typical one-dimensional parameter scan on C-2W involving ten simulations would take 3 days of wall time and require 2.5 million Theta core hours (7.5 million Mira core hours).

Leadership class computing facilities are crucial to this simulation project. To make scientific progress, a week is a practical turnaround time for a parameter scan for FPIC or a linear dispersion scan in ANC. If the computer had 100 times fewer nodes (TAE's commodity cluster has  $\sim 2$  MCH/year), it would be impossible to make progress or execute simulations necessary to support the C-2W campaign.

## I/O Requirements

Typical outputs from a production sized FPIC run consists of mesh and particle snapshots. Mesh snapshots are relatively small with respect to particle snapshots but are saved more frequently. For each production run we anticipate 60 GB and 20 GB of mesh and particle data, respectively. In most cases mesh snapshots do not need to persist in the project directory more than a few weeks. Particle snapshots are retained for at least a few months, to be able to restart partial runs. A parameter scan consisting of 20–30 production runs would result in storage of approximately 600–900 GB. Unlike FPIC, ANC uses a  $\delta f$  representation of the particle distribution, requiring significantly fewer particles per physical volume. Similar to FPIC, 3D mesh snapshots dominate storage requirements, although these are often analyzed in code, reducing them to 2D or even 1D outputs and minimizing IO. Promptly applying analysis can also reduce FPIC mesh data size from 60 to 10 GB or less. A heavy output ANC production run, resulted in 26 GB of total output in storage.



## Computational approach ANC numerical methods

ANC is an electrostatic,  $\delta f$  particle-in-cell simulation code that uses a magnetic field-null-spanning cylindrical coordinate mesh, on which an equilibrium magnetic field, density, and temperatures for each particle species are specified. The axial boundary of this grid is periodic, and the outer radial boundary is reflective to particles, and forced to zero for the Poisson solver. The  $\delta f$  technique, in which an equilibrium particle distribution,  $f$ , is assumed for each species and a perturbation,  $\delta f$ , is dynamically simulated. This technique substantially reduces particle noise at the cost of having to supply an input equilibrium. ANC requires use of the HDF5 library to read in equilibria, numerically specified in the  $R$ - $Z$ -plane. The particle distribution is assumed arbitrary in  $R$ - $Z$ , and may be initialized uniformly or to single harmonic mode in the azimuthal direction. The velocity distribution of the particles is assumed Maxwellian, however, non-Maxwellian distributions may be achieved by superimposing different Maxwellians.

ANC implements both gyrokinetic and fully-kinetic particles in a polymorphic particle type, which is automatically handled in the particle advance routine. The code accommodates three species: ions, electrons, and test particles. Ions may be initialized as gyro or fully-kinetic and electrons may be initialized as gyrokinetic or adiabatic.

## Finite Electron Mass PIC (FPIC) numerical methods

FPIC uses a Cartesian Yee mesh with  $\mathbf{E}, \mathbf{J}, \mathbf{V}, \mathbf{A}$  vector fields defined on the cell edges,  $\mathbf{B}$  field defined on the faces, and densities defined at the vertices. Fully kinetic ions are advanced using the Boris method [*Birdsall and Langdon* (2004)], and their current is deposited in such a way as to respect continuity [*Esirkepov* (2001)], using quadratic spline shaped particles. Electron energy is represented by an equation of state, and a generalized Ohm's law is used with an optional finite electron mass correction term. The Dey-Mittra cut cell method [*Dey and Mittra* (1997)] is used to model shaped conducting boundaries, and boundaries may also be periodic in one or more dimensions. Finite resistivity of the conducting boundary is implemented by coupling free-space exterior solutions to the cut-cell edges. The cut-cell implementation was benchmarked against TEM spherical cavity modes for both conducting and resistive boundaries, and the full PIC code has been benchmarked against normal modes of a cylindrical uniform plasma [*Dettrick, et al.* (2015)] and against the FRC tilt mode [*Ceccherini, et al.* (2016)]. Initial conditions for the code are read from 2D  $(r, z)$  cylindrically symmetric fluid equilibrium models [*Galeotti, et al.* (2011)] and converted to 3D Cartesian representation on the Yee mesh, with Maxwellian particles sampled from the fluid description. Explicit time advance of the field solver is performed by a second order Adams Bashforth method with magnetic field subcycling.

Two other state-of-the-art hybrid PIC codes which have been used to simulate FRCs are the HYM code developed by E. Belova at PPPL [*Belova, et al.* (2001)], and the HYPERS code developed by Y. Omelchenko at Trinum research [*Omelchenko and Karimabadi* (2014)]. Both codes are massively parallel, like FPIC. The HYM code has the advantage of maturity over FPIC, and

has more flexible plasma models, including MHD, MHD+ minority kinetic, and hybrid PIC (like FPIC). The HYPERS code has the advantage of a sophisticated event-driven spatially adaptive time step which allows simulation of a domain where multiple time-scale phenomena are present simultaneously. Of the three codes, FPIC has the most sophisticated boundary model and is the only one with the resistive wall physics that is necessary to model C-2W. HYM and HYPERS are not open source, so from a strategic planning point of view, FPIC is the best option for our community studies.

Both the ANC and the FPIC codes use distributed memory MPI for inter-node parallelism, and both solvers are domain decomposed using PETSc [Balay, *et al.* (2013)]. FPIC is MPI decomposed in 3D using the PETSc DMDA object for simplicity, and the particle set is also 3D decomposed onto the same subdomains, with explicit MPI particle passing used to keep particles on the right MPI rank as they cross subdomain boundaries. Load balancing is complicated because the field solver and the particle push have different optimal domain layouts. This is because the FRC separatrix radius is typically half of the wall radius, so the simulation domain includes a significant volume of low-particle density, typically at least 75% of the volume. Therefore, FPIC uses the particle distribution as the load balance weighting function.

In the ANC case, The Poisson solver is domain decomposed in the  $R$ - $Z$ -plane and spectrally decomposed in the azimuthal coordinate. After decomposing the 3D field into azimuthal harmonics, each harmonic is given its own PETSc solver, which has been pre-initialized before entering the main time-step loop. Particles are group decomposed using MPI, and each MPI process corresponding to a particle group receives a copy of the entire field after the Poisson solve. This does not scale indefinitely with grid size, but is efficient for problem sizes where the field grid fits in memory. Particle domain decomposition will be implemented in ANC for grid sizes above a threshold determined by the architecture memory.

Using the above inter-node parallelism methods, one or more subdomains may be allocated to a single node. Thus a combination of distributed memory and shared memory parallelism can be used for intra-node parallelism. On Theta, both codes use OpenMP to thread the particle push on each MPI subdomain. For FPIC, this approach was developed during an ALCF Director's Discretion allocation on Theta, and was found to scale linearly to 64 cores of one node of Theta.

Field output is performed in parallel using the PETSc HDF5 VecView methods with Vizschema attributes added to enable 3D visualization of staggered Yee mesh quantities in VisIt [Childs, *et al.* (2012)]. For code restart/checkpointing, particle output is performed by direct Parallel HDF5 calls.

ANC's parallelization strategy is largely inherited from GTC, and as such is adaptable to many state of the art parallelization techniques. It will continue to leverage parallelism advances in GTC, including CUDA/OpenACC, and work collaboratively with the GTC team to develop exascale strategies.

## Visualization and analysis for TAE simulations

Interactive 3D VisIt visualization is helpful, but for efficient work flow, it is also crucial to have batch job visualization methods. Our post-processing work-flow tools include automated python scripts that enable batch job 3D VisIt visualization. Another python based batch job visualization tool takes a mid-plane slice view along each axis for all datasets in the output data file. We also have batch scripts for extracting “virtual diagnostics” from the FPIC datasets for apples-to-apples comparison to experimental results.

Because FPIC is 3D and generates a vast amount of data, it is extremely important to find ways to reduce the dimensionality of the data for analysis. One way to do this is through mode analysis, which reduces the 3D data to OD mode amplitudes, from which we compute real frequency and growth rates of instabilities such as internal tilt, radial shift, ballooning, interchange and rotational modes. An example is in Fig. 10.6 where the growth rate of the tilt mode can be derived from the velocity antisymmetry  $v_z^+(r, z) = v_z(r, z) + v_z(r, -z)$ . Reduction of the 3D data to 2D and 1D is possible also. To do this, a field line tracing code which is used to calculate the connection length (from wall to wall) of the field line passing through every point. Iso-surfaces of connection length then provide an approximation to flux surfaces. This is similar to methods used for separatrix identification [Albanese, *et al.* (2015)] in tokamak simulations. The resulting ability to convert some 3D scalar fields, such as density, into approximate 2D and 1D profiles greatly facilitates the comparison of results with theory and allows buildup of intuition. A visualization of the connection length iso-surfaces is shown in Fig. XX.

## Parallel performance

Once the physics parameters for a simulation have been selected, the characteristic length scales such as ion inertial length (FPIC) or electron gyroradius (ANC) set the upper limit on cell size, determining the number of cells. The characteristic times scales such as Alfvén frequency (FPIC) or ion gyrofrequency (ANC) then determine the upper limit on timestep. The goal then is to execute the fixed size simulation as quickly as possible, so strong scaling studies are favored. We demonstrate that FPIC and ANC are computationally ready for Theta, with strong scalings for representative problem sizes showing near ideal performance up to 512 nodes for FPIC, and 2048 nodes for ANC, i.e. 15–30% of the size of Theta.

Other scaling studies show that the point at which the total wall clock time saturates is determined by the number of cells. This field-solver saturation will not be a bottleneck in the context of TAE’s strategic plans, because we will have higher magnetic fields and densities in larger machines. The ion inertial length in prototype reactor conditions is about 4 times smaller than C-2W, meaning that the maximum cell size is about 43 times smaller, and the volume of the domain is at least 10 times bigger, meaning that there would be 640 times as many cells. In such conditions the field solver will saturate at a much higher node count.

### 11.24.7 Development plan for next-generation of TAE systems

Because ANC is closely related to GTC, it will be able to leverage many of the computer science advances that are being developed in the CAAR program and the SummitDev preparations for Summit. ANC's development for next generation systems will largely rest on top of these significant public investments in GTC development. FPIC parallelization plans for next generation systems include improving load balance by replacing the PETSc DMDA representation with a more general decomposition based on the PETSc Index Set (IS) and Application Ordering (AO) concepts. Both codes will experiment with porting the OpenMP methods developed on KNL to OpenACC methods for deployment on GPU, for next generation systems that use accelerators. I/O performance could be a significant limiting factor for both codes on next generation systems, so we are exploring the possibility of leveraging recent ASCR funded advances in in-situ visualization such as the SENSEI project [*Ayachit, et al.* (2016)].

# Bibliography

- [1] Albanese, R., De Magistris, M., Fresa, R., Maviglia, F. and Minucci, S. (2015). Accuracy assessment of numerical tracing of three-dimensional magnetic field lines in tokamaks with analytical invariants, *Fusion Sci. Tech.* **68**, pp. 741–749, <https://doi.org/10.13182/FST15-127>.
- [2] Ayachit, U., Whitlock, B., Wolf, M., Loring, B., Geveci, B., Lonie, D. and Bethel, E. Wes (2016). The SENSEI generic in situ interface, 2016 Second Workshop on In Situ Infrastructures for Enabling Extreme-Scale Analysis and Visualization (ISAV), 13 Nov. 2016, Salt Lake City, UT, USA, <https://doi.org/10.1109/ISAV.2016.013>.
- [3] Balay, S., Brown, J., Buschelman, K., Eijkhout, V. *et al.* (2013). PETSc Users Manual.
- [4] Barnes, D. C. and Milroy, R. D. (1991). Stabilization of the Field-Reversed Configuration (FRC) tilt instability with energetic ion beams, *Phys. Fluids B: Plasma Phys.* **3**, p. 2609, <https://doi.org/10.1063/1.859973>.
- [5] Belova, E. V., Jardin, S., Ji, H., Yamada, M. and Kulsrud, R. (2001). Numerical study of global stability of oblate field-reversed configurations, *Phys. Plasmas* **8**, p. 1267, <https://doi.org/10.1063/1.1355027>.
- [6] Belova, E. V., Davidson, R. C., Ji, H. and Yamada, M. (2003). Kinetic effects on the stability properties of field-reversed configurations. I. Linear Stability, *Phys. Plasmas* **10**, p. 2361, <https://doi.org/10.1063/1.1568118>.
- [7] Belova, E. V., Davidson, R. C., Ji, H. and Yamada, M. (2004). Kinetic effects on the stability properties of field-reversed configurations. II. Nonlinear evolution, *Phys. Plasmas* **11**, pp. 2523–2531, <https://doi.org/10.1063/1.1666293>.
- [8] Belova, E. V. (2015). Beam ion effects on FRC stability, 57th Annual Meeting of the APS Division of Plasma Physics, November 16–20, 2015, Savannah, Georgia, <http://meetings.aps.org/link/BAPS.2015.DPP.BP12.9>.
- [9] Binderbauer, M. W., Tajima, T., Steinhauer, L. C., Garate, E., Tuszewski, M., Schmitz, L., Guo, H. Y., Smirnov, A., Gota, H., Barnes, D., Deng, B. H., Thompson, M. C., Trask, E., Yang, X., Putvinski, S., Rostoker, N., Andow, R., Aefsky, S., Bolte, N., Bui, D. Q., Ceccherini, F., Clary, R., Cheung, A. H., Conroy, K. D., Dettrick, S. A., Douglass, J.

- D., Feng, P., Galeotti, L., Giammanco, F., Granstedt, E., Gupta, D., Gupta, S., Ivanov, A. A., Kinley, J. S., Knapp, K., Korepanov, S., Hollins, M., Magee, R., Mendoza, R., Mok, Y., Necas, A., Primavera, S., Onofri, M., Osin, D., Rath, N., Roche, T., Romero, J., Schroeder, H., Sevier, L., Sibley, A., Song, Y., Van Drie, A. D., Walters, J. K., Waggoner, W., Yushmanov, P., Zhai, K., and the TAE Team (2015). A high-performance field-reversed configuration, *Phys. Plasmas* **22**, p. 056110, <http://dx.doi.org/10.1063/1.4920950>.
- [10] Birdsall, C. K. and Langdon, A. B. (2004). *Series in Plasma Physics* (Taylor and Francis Group), ISBN:9780750310253.
- [11] Caldas, I. L., Marcus, F. A., Batista, A. M., Viana, R. L., Lopes, S. R., Heller, M. V. A. P., Guimarães-Filho, Morrison, P. J. and Horton, W. (2006). Turbulence induced transport in tokamaks, *AIP Conf. Proceedings* **875**, p. 341, <https://doi.org/10.1063/1.2405962>.
- [12] Ceccherini, F., Dettrick, S., Barnes, D., Galeotti, L. and TAE Team (2016). FPIC Study of the  $n = 1$  Toroidal Mode in FRC Plasmas, 58th Annual Meeting of the APS Division of Plasma Physics, Vol. 61, Number 18, October 31–November 4 2016; San Jose, California, <http://meetings.aps.org/link/BAPS.2016.DPP.CP10.87>.
- [13] Chang, C. S. and Ku, S. (2008). Spontaneous rotation sources in a quiescent tokamak edge plasma, *Phys. Plasmas* **15**, p. 062510, <https://doi.org/10.1063/1.2937116>.
- [14] Childs, H., Brugger, E., Whitlock, B. Meredith, J., Ahern, S., Pugmire, D., Biagas, K., Miller, M., Harrison, C., Weber, G. H., Krishnan, H., Fogal, T., Sanderson, A., Garth, C., Bethel, E. W., Camp, D., Rübel, O., Durant, M., Favre, J. and Navratil, P. (2012). VisIt: An end-user tool for visualizing and analyzing very large data, Lawrence Berkeley National Laboratory, <https://escholarship.org/uc/item/69r5m58v>.
- [15] Dettrick, S., Barnes, D., Ceccherini, F., Galeotti, L., Guerrero, V., Hendrix, D., Hubbard, K., Milroy, R., Necas, A. and TAE Team (2015). FPIC: A Key Next Step for Stability Studies of Advanced Beam Driven FRCs, 57th Annual Meeting of the APS Division of Plasma Physics. Vol. 60, Number 19, November 16–20, 2015, Savannah, Georgia, <http://meetings.aps.org/link/BAPS.2015.DPP.BP12.31>.
- [16] Dey, S. and Mittra, R. (1997). locally conformal finite-difference time-domain (FDTD) algorithm for modeling three-dimensional perfectly conducting objects, *IEEE Microwave and Guided Wave Lett.* **7**, pp. 273–275, <https://doi.org/10.1109/75.622536>.
- [17] Dong, J-Q., Mahajan, S. M. and Horton, W. (1997). Coupling of  $\eta_i$  and trapped electron modes in plasmas with negative magnetic shear, *Phys. Plasmas* **4** p. 755, <https://doi.org/10.1063/1.872169>.
- [18] Dong, J-Q., Horton, W., Bengtson, Roger D. and Li, G. X. (1998). Momentum-energy transport from turbulence driven by parallel flow shear, *Phys. Plasmas* **1**, p. 3250, <https://doi.org/10.1063/1.870477>.

- [19] Dongarra, J. (2013). International HPC Forum (IHPCF), Changsha, China, May 28–29, 2013.
- [20] Donovan, E., Liu, W., Liang, J., Spanswick, E., Voronkov, I., Connors, M., Syrjäsuo, M., Baker, G., Jackel, B., Trondsen, T., Greffen, M., Angelopoulos, V., Russell, C. T., Mende, S. B., Frey, H. U., Keiling, A., Carlson, C. W., McFadden, J. P., Glassmeier, K–H., Auster, U., Hayashi, K., Sakaguchi, K., Shiokawa, K., Wild, J. A. and Rae, I. J. (2008). Simultaneous THEMIS in situ and auroral observations of a small substorm. *Geophys. Res. Lett.* **35**, p. L17S18, <https://doi.org/10.1029/2008GL033794>.
- [21] Esirkepov, T. Zh. (2001). Exact charge conservation scheme for particle–in–cell simulation with an arbitrary form–factor, *Comp. Phys. Comm.* **135**, pp. 144–153, [https://doi.org/10.1016/S0010-4655\(00\)00228-9](https://doi.org/10.1016/S0010-4655(00)00228-9).
- [22] Fu, X. R., Horton, W., Xiao, Y., Lin, Z., Sen, A. K. and Sokolov, V. (2012). Validation of electron temperature gradient turbulence in the Columbia Linear Machine, *Phys. Plasmas* **19**, p. 032303, <https://doi.org/10.1063/1.3686148>.
- [23] Fujita, T., Kamada, Y., Ishida, S., Neyatani, Y., Oikawa, T., Ide, S., Takeji, S., Koide, Y., Isayama, A., Fukuda, T., Hatae, T., Ishii, Y., Ozeki, T., Shirai, H. and JT–60 Team. (1999). High performance experiments in JT–60U reversed shear discharges, *Nucl. Fusion* **39**, p. 1627, <http://iopscience.iop.org/0029-5515/39/11Y/302>.
- [24] Fulton, D. P., Lau, C. K., Schmitz, L., Holod, I., Lin, Z., Tajima, T., Binderbauer, M.W. and TAE Team. (2016). Gyrokinetic simulation of drift wave instability in field–reversed configuration, *Phys. Plasmas* **23**, p. 056111, <https://doi.org/10.1063/1.4948285>.
- [25] Futatani, S., Horton, W., Benkadda, S., Bespamyatnov, I. O. and Rowan, W. L. (2010). Fluid models of impurity transport via drift wave turbulence, *Phys. Plasmas* **17**, p. 072512, <http://dx.doi.org/10.1063/1.3459062>.
- [26] Galeotti, L., Barnes, D., Ceccherini, F. and Pegoraro, F. (2011). Plasma equilibria with multiple ion species: Equations and algorithm, *Phys. Plasmas* **18**, p. 082509, <https://doi.org/10.1063/1.3625275>.
- [27] Hazeltine, R. (2009). Research needs for magnetic fusion energy sciences, Report of the Research Needs Workshop (ReNeW), U. S. Department of Energy (Washington, DC).
- [28] Hill, D. (2008). Report of the FESAC Toroidal Alternates Panel, USDOE, Washington, D.C.
- [29] Holod, I., Zhang, W. L., Xiao, Y., and Lin, Z. H. (2009). Electromagnetic formulation of global gyrokinetic particle simulation in toroidal geometry, *Phys. Plasmas* **16**, p. 122307, <https://dx.doi.org/10.1063/1.3273070>.
- [30] Horton, W., Hong, B.–G. and Tang, W. M. (1988). Toroidal electron temperature gradient driven drift modes, *Phys. Fluids* **31**, p. 2971–2983, <http://dx.doi.org/10.1063/1.866954>.

- [31] Horton, W. (1989). Drift wave vortices and anomalous transport, *Phys. Fluids B* **1**, p. 524, <https://doi.org/10.1063/1.859168>.
- [32] Horton, W. and Hasegawa, A. (1994). Quasi-two-dimensional dynamics of plasmas and fluids, *Chaos* **4**, p. 227, <https://doi.org/10.1063/1.166049>.
- [33] Horton, W. and Rowan, W. (1994). Impurity transport studies in the Texas Experimental Tokamak (TEXT), *Phys. Plasmas* **1**, p. 901, <https://doi.org/10.1063/1.870749>.
- [34] Horton, W., Tajima, T., Dong, J-Q., Kim, J-Y., and Kishimoto, Y. (1997). Ion transport analysis of a high-beta poloidal JT60-U discharge, *Plasma Phys. Control. Fusion* **39**, pp. 83–104, <https://doi.org/10.1088/0741-3335/39/1/006>.
- [35] Horton, W., Park, H-B., Kwon, J-M., Strozzi, D., Morrison, P. J. and Choi, D-I. (1998). Drift wave test particle transport in reversed shear profile, *Phys. Plasmas* **5**, p. 3910, <https://doi.org/10.1063/1.873110>.
- [36] Horton, W., Zhu, P., Hoang, G. T., Aniel, T., Ottaviani, M. and Garbet, X. (2000). Electron transport in tore supra with fast wave electron heating, *Phys. Plasmas* **7**, pp. 1494–1511, <http://dx.doi.org/10.1063/1.873969>.
- [37] Horton, W., Hoang, G. T., Bourdelle, C., Garbet, X., Ottaviani, M., and Colas, L. (2004). *Phys. Plasmas* **11**, p. 2600, <http://dx.doi.org/10.1063/1.69076>.
- [38] Horton, W., Wong, H. V., Morrison, P. J., Wurm, A., Kim, J. A., Perez, J. C., Pratt, J., Hoang, G. T., LeBlanc, B. P. and Ball, R. (2005). Temperature gradient driven electron transport in NSTX and Tore Supra, *Nucl. Fusion* **45**, p. 976, <https://doi.org/10.1088/0029-5515/45/8/025>.
- [39] Horton, W., Fu, X. R. and Beklemishev, A. (2010). Parameter optimization studies for a tandem mirror neutron source, *J. Fusion Energy* **29**, pp. 521–526, <https://doi.org/10.1007/s10894-010-9332-9>.
- [40] Hu, G. and Krommes, J. A. (1994). Generalized weighting scheme for  $\delta f$  particle-simulation method, *Phys. Plasmas* **1**, p. 863, <https://doi.org/10.1063/1.870745>.
- [41] Hu, G. and Horton, W. (1997). Minimal model for transport barrier dynamics based on ion-temperature-gradient turbulence, *Phys. Plasmas* **4**, pp. 3262–3272, <https://doi.org/10.1063/1.872467>.
- [42] Ishida, S., Fujita, T., Akasaka, H., Akino, N., Annou, K., Aoyagi, T., Arai, T., Arakawa, K., Asakura, N., Azumi, M., Budny, R., Chiba, S., Da Costa, O., Ebisawa, N., Fujii, T., Fukuda, T., Funahashi, A., Grisham, L., Gunji, S., Hamamatsu, K., Hiratsuka, H., Hirauchi, S., Hirayama, T., Honda, A., Honda, M., Hosogane, N., Ichige, H., Ide, S., Ikeda, Y., Isaka, M., Isayama, A., Isei, N., Ishii, Y., Isozaki, N., Itami, K., Itoh, T., Iwahashi, T., Kamada, Y., Kaminaga, A., Kashiwabara, T., Kawai, M., Kawamata, Y., Kawano, Y., Kazama,



- D., Kazawa, M., Kikuchi, M., Kimura, H., Kimura, T., Kishimoto, H., Kishimoto, Y., Kitamura, S., Kiyono, K., Kodama, K., Koide, Y., Kokusen, S., Kondoh, T., Konoshima, S., Koog, J., Kramer, G. J., Kubo, H., Kurihara, K., Kurita, G., Kuriyama, M., Kusama, Y., Masaki, K., Matsuda, T., Matsumoto, T., Matukawa, M., Miura, T., Miya, N., Miyachi, K., Miyata, H., Miyo, Y., Mogaki, K., Mori, M., Morimoto, M., Morioka, S., Moriyama, S., Nagami, M., Nagashima, A., Nagashima, K., Nagaya, S., Naito, O., Nakamura, Y., Nemoto, M., Neyatani, Y., Nishitani, T., Ogiwara, N., Ohga, T., Ohsawa, M., Ohshima, T., Oikawa, T., Okabe, T., Okano, J., Omori, K., Omori, S., Omori, Y., Onose, Y., Oohara, H., Ozeki, T., Saidoh, M., Saigusa, M., Saito, N., Sakasai, A., Sakata, S., Sakurai, S., Sasajima, T., Sato, M., Scott, S. D., Seimiya, M., Seiki, H., Seki, M., Shimada, M., Shimizu, K., Shimizu, M., Shimono, M., Shinozaki, S., Shirai, H., Shitomi, M., Suganuma, K., Sugie, T., Sunaoshi, H., Takahashi, M., Takahashi, S., Takeji, S., Takenaga, H., Takizuka, T., Tamai, H., Terakado, M., Terakado, T., Tobita, K., Tokuda, S., Totsuka, T., Toyokawa, Y., Toyoshima, N., Tsuchiya, K., Tsugita, T., Tsukahara, Y., Tuda, T., Uramoto, Y., Ushigusa, K., Usui, K., Yagyu, J., Yamagiwa, M., Yamamoto, M., Yamamoto, T., Yamashita, O., Yokokura, K., Yoshida, H., Yoshida, M. and Yoshino, R. (1997). Achievement of high-fusion performance in JT60-U reversed shear discharges, *Phys. Rev. Lett.* **79**, p. 3917, <https://doi.org/10.1103/PhysRevLett.79.3917>.
- [43] Ivanov, A. A. and Prikhodko, V. V. (2013). Gas-dynamic trap: an overview of the concept and experimental results, *Plasma Phys. Control. Fusion* **55**, p. 63001, <https://doi.org/10.1088/0741-3335/55/6/063001>.
- [44] Kaye, S. M., Levinton, F. M., Stutman, D., Tritz, K., Yuh, H., Bell, M. G., Bell, R. E., Domier, C. W., Gates, D., Horton, W., Kim, J-Y., LeBlanc, B. P., Luhman, Jr., N. C., Maingi, R., Mazzucato, E., Menard, J. E., Mikkelsen, D., Mueller, D., Park, H., Rewoldt, G., Sabbagh, S. A., Smith, D. R. and Wang, W. (2007). Confinement and local transport in the National Spherical Torus Experiment (NSTX), *Nucl. Fusion* **47**, p. 499, <http://dx.doi.org/10.1088/0029-5515/47/7/001>.
- [45] Kaye, S. M., Gerhardt, S., Guttenfelder, W., Maingi, R., Bell, R. E., Diallo, A., LeBlanc, B. P. and Podesta, M. (2013). The dependence of H-mode energy confinement and transport on collisionality in NSTX, *Nucl. Fusion* **53**, p. 063005, <https://doi.org/10.1088/0029-5515/53/6/063005>.
- [46] Lau, C. K., Fulton, D. P., Holod, I., Lin, Z., Binderbauer, M., Tajima, T. and Schmitz, L. (2017). Drift-wave stability in the field-reversed configuration, *Phys. Plasmas* **24**, p. 082512, <https://doi.org/10.1063/1.4993630>.
- [47] Li, J. and Kishimoto, Y. (2002). Interaction between small-scale zonal flows and large-scale turbulence: A theory for ion transport intermittency in tokamak plasmas, *Phys. Rev. Lett.* **89**, pp. 115002–1, <https://doi.org/10.1103/PhysRevLett.89.115002>.

- [48] Lin, Z., Ethier, S., Hahm, T. S. and Tang, W. M. (2002). Size scaling of turbulent transport in magnetically-confined plasmas, *Phys. Rev. Lett.* **88**, p. 195004, <https://doi.org/10.1103/PhysRevLett.88.195004>.
- [49] Mazzucato, E., Smith, D. R., Bell, R. E., Kaye, S. M., Hosea, J. C., LeBlanc, B. P., Wilson, J. R., Ryan, P. M., Domier, C. W., Luhmann, Jr., N. C., Yuh, H., Lee, W. and Park, H. (2008). *Phys. Rev. Lett.* **101**, p. 075001, <https://doi.org/10.1103/PhysRevLett.101.075001>.
- [50] Mazzucato, E., Bell, R. E., Ethier, S., Hosea, J. C., Kaye, S. M., LeBlanc, B. P., Lee, W. W., Ryan, P. M., Smith, D. R., Wang, W. X., Wilson, J. R. and Yuh, H. (2009). Study of turbulent fluctuations driven by the electron temperature gradient in the National Spherical Torus Experiment, *Nucl. Fusion* **49**, p. 055001, <https://doi.org/10.1088/0029-5515/49/5/055001>.
- [51] Meng, X., Zhu, X., Wang, P., Zhao, Y., Liu, X., Zhang, B., Xiao, Y., Zhang, W. and Lin, Z. (2013). Heterogeneous programming and optimization of gyrokinetic toroidal code and large-scale performance test on TH-1A, in International Supercomputing Conference, 2013, pp. 81–96, [https://doi.org/10.1007/978-3-642-38750-0\\_7](https://doi.org/10.1007/978-3-642-38750-0_7).
- [52] Milroy, R. D., Barnes, D. C., Bishop, R. C. and Webster, R. B. (1989). Nonlinear magneto-hydrodynamic studies of the tilt mode in field configurations, *Phys. Fluids B: Plasma Phys.* **1**, p. 1225, <https://doi.org/10.1063/1.858998>.
- [53] Milroy, R. D., Macnab, A. I. D., Kim, C. C. and Sovinec, C. R. (2008). FRC Simulations using the NIMROD Code, *J. Fusion Energy* **27**, pp. 73–76, <https://doi.org/10.1007/s10894-007-9089-y>.
- [54] Omelchenko, A. and Karimabadi, H. (2014). Parallel asynchronous hybrid simulations of strongly inhomogeneous plasmas, Proceedings of the Winter Simulation Conference, pp. 3435–3446, <http://dx.doi.org/10.1109/WSC.2014.7020176>.
- [55] Parks, P. B. and Schaffer, M. J. (2003). Analytical equilibrium and interchange stability of single- and double-axis field-reversed configurations inside a cylindrical cavity, *Phys. Plasmas* **10**, p. 1411, <https://doi.org/10.1063/1.1566025>.
- [56] Rosenbluth, M. N., Krall, N. A. and Rostoker, N. (1962). Finite Larmor radius stabilization of “weakly” unstable confined plasmas, *Nucl. Fusion Suppl.* **143**, OSTI ID:4808729.
- [57] Rowan, W. L., Bespamyatnov, Igor O. and Fiore, C. L. (2008). Light impurity transport at an internal transport barrier in Alcator C-Mod, *Nucl. Fusion* **48**, p. 105005, <https://doi.org/10.1088/0029-5515/48/10/105005>.
- [58] Ryutov, D. D. (1990). Mirror type neutron source, *Plasma Phys. Control. Fusion* **32**, p. 999, <https://doi.org/10.1088/0741-3335/32/11/012>.

- [59] Schmitz, L., Fulton, D. P., Ruskov, E., Lau, C., Deng, B. H., Tajima, T., Binderbauer, M. W., Holod, I., Lin, Z., Gota, H., Tuszewski, M., Dettrick, S. A. and Steinhauer, L. C. (2016). Suppressed ion-scale turbulence in a hot high- $\beta$  plasma, *Nature Comm.* **7**, p. 13860, <https://doi.org/10.1038/ncomms13860>.
- [60] Schmitz, L., Ruskov, E., Deng, B. H., Binderbauer, M., Tajima, T., Gota, H., Tuszewski, M. and the TAE Team (2016). Control of ion gyroscale fluctuations via electrostatic biasing and sheared  $\mathbf{E} \times \mathbf{B}$  flow in the C-2 field reversed configuration, *AIP Conference Proceedings* **1721**, <http://dx.doi.org/10.1063/1.4944018>.
- [61] SciDAC Project, Whole Device Modeling of Compact Tori. submitted (Funding Opportunity Announcement DE-FOA-0001670 , Tracking Number GRANT12349965) (2017).
- [62] Sen, A. K., Chen, J. and Mael, M. (1991). Production and identification of the ion-temperature-gradient instability, *Phys. Rev. Lett.* **66**, pp. 429–432, <http://dx.doi.org/10.1103/PhysRevLett.66.429>.
- [63] Slusher, R. E. and Surko, C. M. (1978). Study of density fluctuations in the absorption of oxygen on silicon, *Phys. Rev. Lett.* **40**, p. 400, <https://doi.org/10.1103/PhysRevLett.40.400>, Erratum *Phys. Rev. Lett.* **40**, p. 593.
- [64] Steinhauer, Loren C. (2011). Review of field-reversed configurations, *Phys. Plasmas* **18**, p. 070501, <http://dx.doi.org/10.1063/1.3613680>.
- [65] Stone, E., Cummings, A. C., Heikkila, B. C. and Lal, N. (2019). Cosmic ray measurements from Voyager 2 as it crossed into interstellar space, *Nature Astron.* **3**, pp. 1013–1018, <https://doi.org/10.1038/s41550-019-0928-3>.
- [66] Sudo, S., Tamura, N., Suzuki, C., Muto, S., Funaba, H. and LHD Group (2012). Multiple-tracer TESPEL injection for studying impurity behavior in a magnetically-confined plasma, *Nucl. Fusion* **52**, p. 063012, <http://dx.doi.org/10.1088/0029-5515/52/6/063012>.
- [67] Tajima, T. and Asai, T. (2016). US-Japan Workshop on Compact Torus.
- [68] Xiao, Y. and Lin, Z. (2009). Turbulent transport of trapped-electron modes in collisionless plasmas, *Phys. Rev. Lett.* **103**, p. 085004, <https://doi.org/10.1103/PhysRevLett.103.085004>.
- [69] Yamada, M., Ji, H., Gerhardt, S. P., Belova, E. V., Davidson, R. C. and Mikkelsen, D. R. (2007). A self-organized plasma with induction, reconnection, and injection techniques: the SPIRIT concept for field reversed configuration research, *Plasma Fusion Res.* **2**, p. 4, <https://doi.org/10.1585/pfr.2.004>.
- [70] Yoshinuma, M., Ida, K., Yokoyama, M., Osakabe, M. and Nagaoka, K. (2010). Charge-exchange spectroscopy with pitch-controlled double-slit fiber bundle on LHD, *Fusion Sci. Tech.* **58**, pp. 375–382, <https://doi.org/10.13182/FST10-A10823>.